

# MHD mixed convection of viscoplastic fluids in different aspect ratios of a lid-driven cavity using LBM

GH. R. Kefayati\*, H. Tang

*Department of Mechanical Engineering, The Hong Kong Polytechnic University, Kowloon, Hong Kong*

---

## Abstract

In this paper, a two-dimensional simulation of mixed convection in an enclosure with differentially heated sidewalls in the presence of a uniform magnetic field has been performed for different aspect ratios of the enclosure while the enclosure is filled with a viscoplastic fluid. The viscoplastic fluid has been simulated by the exact Bingham model without any regulations. Lattice Boltzmann Method (LBM) has been applied to solve the problem. Heat transfer, fluid flow, and yielded/unyielded zones are investigated for certain pertinent parameters of the Reynolds number ( $Re = 100, 500, \text{ and } 1000$ ), the Hartmann number ( $Ha = 0, 2, \text{ and } 5$ ), the Bingham number ( $Bn = 1, 5, \text{ and } 10$ ), the aspect ratio ( $AR = 0.25, 1, \text{ and } 4$ ), and Eckert number ( $Ec = 0, 10^{-4}, 10^{-3}, \text{ and } 10^{-2}$ ) when the Grashof and Prandtl numbers are fixed at  $Gr = 10^4$  and  $Pr = 1$ ; respectively. Results show that the increase in the Reynolds number augments the heat transfer and changes the extent of the unyielded section. Furthermore, for fixed studied parameters, an increase in the Bingham number decreases the heat transfer while enlarging the unyielded section. The rise of the aspect ratio alters the size and position of the unyielded/yielded zones. As Hartmann number rises, the heat transfer drops gradually and the unyielded parts increase significantly. The change of the magnetic field angle alters the heat transfer and the unyielded/yielded regions in the cavity. It was observed that the viscous dissipation and the joule heating parts in the energy equation based on the practical values of Eckert numbers have marginal effects on heat transfer and yielded/unyielded sections.

*Key words:* Mixed convection, MHD, viscoplastic fluid, lid-driven cavity, Lattice Boltzmann method

---

\* Corresponding author. Dr. Gholamreza Kefayati (GH. R. Kefayati)  
*Email addresses:* gholamrezakefayati@gmail.com,  
gholamreza.kefayati@polyu.edu.hk (GH. R. Kefayati), h.tang@polyu.edu.hk (H. Tang).

# 1 Introduction

## 1.1 Magnetohydrodynamics

Magnetic field is widely utilized on materials which show viscoplastic behavior in different industries such as cement and food industries [1,2]. Magnetohydrodynamics (MHD) is the study of the interaction between magnetic fields and moving, conducting fluids. Magnetic fields influence many natural and man-made flows. They are routinely used in industry to heat, pump, stir and levitate liquid metals. There are three types of magnetic fields; a terrestrial magnetic field which is maintained by fluid motion in the earth's core, a solar magnetic field, which generates sunspots and solar flares, and a galactic field which influences the formation of stars. When a constant current is injected into a fluid under the influence of a magnetic field, the resulting Lorentz force will, in general, produce motion. Electromagnetic pumps were one of the earliest applications of MHD, and were routinely used in various industries [3]. Fluid flow and heat transfer analysis in lid-driven cavities is one of the most widely studied problems in thermo-fluids area. Numerous investigations have been conducted in the past on lid-driven cavity flow and heat transfer considering various combinations of the imposed temperature gradients and cavity configurations [4–15]. This is because the driven cavity configuration is encountered in many practical engineering and industrial applications, e.g., materials processing, flow and heat transfer in solar ponds, dynamics of lakes, reservoirs and cooling ponds, crystal growing, float glass production, metal casting, food processing, galvanizing, and metal coating, etc.

## 1.2 MHD on natural and mixed convection of Newtonian fluids

MHD natural and mixed convection of Newtonian fluids in a cavity with different boundary conditions have been studied widely by researchers. Sathiyamoorthy and Chamkha [16] have done a numerical study for natural convection flow of electrically conducting liquid gallium in a square cavity whereas the bottom wall is uniformly heated and the left and right vertical wall is linearly heated while the top wall kept thermally insulated. They exhibited that the magnetic field with inclined angle has effects on the flow and heat transfer rates in the cavity. Number of investigators which effects of MHD mixed convection in lid-driven cavities is very limited. Sivasankaran et al. [17] investigated mixed convection in a square cavity of sinusoidal boundary temperatures at the sidewalls in the presence of magnetic field numerically. Rahman et al. [18] studied the development of magnetic field effect on mixed convective flow in

a horizontal channel with a bottom heated open enclosure. Their results indicate that various Hartmann, Rayleigh and Reynolds numbers strongly affect the flow phenomenon and temperature field inside the cavity whereas in the channel these effects are less significant. Oztop et al. [19] considered laminar mixed convection flow in the presence of magnetic field in a top sided lid-driven cavity heated by a corner heater. They exhibited heat transfer decreases with increasing of Hartmann number. Nasrin and Parvin [20] made a numerical work on Hydromagnetic effect on mixed convection in a lid-driven cavity with sinusoidal corrugated bottom surface. They indicated that the average Nusselt number at the heated surface increases with an increase of the number of waves as well as the Reynolds number, while decreases with increment of Hartmann number. Kefayati et al. [21] simulated mixed convection of MHD in a lid-driven cavity by a linearly heated wall, using LBM. They studied different parameters of Hartmann numbers, Richardson numbers, and the inclinations of the magnetic field. Effects of a magnetic field on mixed convection flow in a two-sided lid-driven cavity were analyzed, using Lattice Boltzmann method (LBM) by Sajjadi et al. [22]. Results demonstrated that the heat transfer augmented with an increment of the Richardson number for different Hartmann numbers. In addition, the heat transfer declined with the growth of the magnetic field for various Richardson numbers. Sajjadi et al. [23] used the lattice Boltzmann method to solve the turbulent and laminar MHD natural convection in a square cavity. In this paper a fluid with  $Pr = 6.2$  and different Rayleigh numbers for laminar and turbulent flows in the presence of a magnetic field was investigated. Ashorynejad et al. [24] presented a numerical study about the effect of a uniform magnetic field on free convection in a horizontal cylindrical annulus using the lattice Boltzmann method. The inner and outer cylinders were maintained at uniform temperatures and it was assumed the walls were insulating with a magnetic field. Detailed numerical results of heat transfer rate, temperature, and velocity fields were presented for studied parameters. Ashorynejad et al. [25] investigated the effect of static radial magnetic field on natural convection heat transfer in a horizontal cylindrical annulus enclosure filled with nanofluid numerically using the Lattice Boltzmann method (LBM). The inner and outer cylinder surfaces were maintained at the different uniform temperatures. The surfaces were non-magnetic material. The investigation was carried out for different governing parameters namely, Hartmann number, nanoparticle volume fraction and Rayleigh number. Yousofvand et al. [26] analyzed MHD mixed convection inside an electromagnetic pump, with Cu-water nanofluid as the working fluid numerically. To find the best heat transfer and pumping performance, an in-house parallel lattice Boltzmann code was developed to solve the problem in a 3D domain. The study was conducted for the certain pertinent parameters of Rayleigh number, magnetic field strength, electric field strength and the nanoparticle volume fraction. Mehryan et al. [27] investigated numerically the problem of unsteady natural convection inside a square cavity partitioned by a flexible impermeable membrane. The finite element method with the arbi-

trary Lagrangian-Eulerian (ALE) technique was used to model the interaction of the fluid and the membrane. The horizontal walls of the cavity were kept adiabatic while the vertical walls were kept isothermal at different temperatures. A uniform magnetic field was applied onto the cavity with different orientations. The cavity was provided by two eyelets to compensate volume changes due the movement of the flexible membrane. Ghalambaz et al. [28] studied the MHD phase change heat transfer of a phase change substance in the presence of a uniform magnetic field theoretically in a cavity. A fixed grid method associated with the enthalpy-porosity method was utilized. The governing equations were transformed into a non-dimensional form and solved using the finite element method. The impacts of the crucial parameters such as the Hartmann number and the inclination angle on the phase change process were investigated. Selimefendigil and Oztop [29] performed a numerical study of MHD mixed convection nanofluid filled lid driven square enclosure. The bottom wall of the cavity was heated and the top wall was kept at constant temperature lower than that of the heater. Other walls of the square enclosure and cylinder surface were assumed to be adiabatic. The governing equations were solved with finite element method. Selimefendigil and Oztop [30] investigated natural convection in a CuO-water nanofluid filled horizontal partitioned annulus formed by two isothermal surfaces under the influence of an inclined magnetic field was numerically. A conductive partition with varying thickness and thermal conductivity was placed within the annulus. Finite element method was utilized to solve the governing equations. Bondareva and Sheremet [31] studied natural convective heat transfer combined with melting in a cubical cavity filled with a pure gallium under the effects of inclined uniform magnetic field and local heater numerically. The domain of interest was an enclosure bounded by two isothermal opposite vertical surfaces of low constant temperature and adiabatic other walls. A heat source of constant temperature was located on the bottom wall. Gibanov et al. [32] analysed MHD mixed convection in a lid-driven cavity with partially filled with a porous medium saturated with a ferrofluid numerically. The domain of interest consists of a bottom porous layer and a nanofluid layer over the porous one with a heated motionless bottom wall and cooled upper moved wall. The governing partial differential equations formulated on the basis of a single-phase model for nanofluid, Brinkman-extended Darcy model for porous layer and Boussinesq approximation for buoyancy force solved by finite difference method of the second-order accuracy. Son and Park et al. [33], numerically, investigated the two-dimensional laminar natural convection in a differently heated rectangular enclosure with an insulated square block, in the presence of a uniform magnetic field applied in the horizontal direction. Numerical simulations were performed for the conditions of different Rayleigh and Hartmann numbers with a fixed Prandtl number. Hatami et al. [34] studied the effect of a variable magnetic field (VMF) on the natural convection heat transfer of Fe<sub>3</sub>O<sub>4</sub>-water nanofluid in a half-annulus cavity by finite element method using FlexPDE commercial code. After deriving the governing equations and

solving the problem by defined boundary conditions, the effects of three main parameters (Hartmann number, nanoparticles volume fraction and Rayleigh number) on the local and average Nusselt numbers of inner wall were investigated. Some other studies in this area can be observed in [35–42].

### *1.3 Viscoplastic fluids*

Fluids, which are used in different engineering applications, can be classified into two groups namely Newtonian and non-Newtonian depending on their behavior under shear stress. The example of non-Newtonian fluids is abundant in nature, biological as well as man-made systems. Common examples can be found in petroleum and chemical industries, food processing, material and polymer fabrication and bio medical applications. Several idealized mathematical models have been proposed to represent the behavior of non-Newtonian fluids. Power law model is generally used to represent a class of non-Newtonian fluids which are inelastic and exhibit time independent shear stress. Another main class of non-Newtonian fluid is visco-plastic liquids which due to the ability of them to sustain a certain external load without significant deformations in contrast with common fluids is an important and challenging problem. In fact, below a certain stress yield, the medium enjoys rigidity; above this yield the medium behaves like an incompressible viscous fluid. The direct consequence of this property is that the flow field is divided into two regions: the unyielded and the yielded zone. A profound knowledge of the location and shape of the yield surface, i.e. the interface between these two sets, is essential in solving the flow problems of such fluids. Some popular materials which show this behavior are fresh concrete, cement, mayonnaise, tortilla dough, fruits-syrup mixtures, blood in the capillaries, muds used in drilling technologies and tooth pastes [43].

### *1.4 Viscoplastic fluids in an isothermal lid-driven cavity*

The visco-plastic fluids have been simulated in an isothermal lid-driven cavity with different methods and regularizations. Sanchez [44] applied a first-order operator splitting method for modeling of a Bingham visco-plastic medium in a lid-driven cavity. Dean and Glowinski [45] discussed a computational method for the numerical simulation of unsteady Bingham visco-plastic fluid based on time-discretization by operator splitting method. Moreover, they illustrated the result of the method for the Bingham visco-plastic fluid in a lid-driven cavity. Mitsoulis and Zisis [46] studied Bingham visco-plastic fluid in a lid-driven cavity using the Papanastasiou modification to the ideal Bingham model. Neofytou [47] simulated Bingham flows in a lid-driven cavity, utilizing

Papanastasiou model. They exhibited streamlines and velocities in the middle of cavity in the investigation. Vola et al. [48] proposed a numerical method to calculate unsteady flows of Bingham fluids without any regularization of the constitutive law. They illustrated the applied numerical strategy through two well-known problems, namely the hydrodynamic benchmark of the lid-driven cavity and the natural convection benchmark of the differentially heated cavity. Huilgol and You [49] reviewed a summary of the development of the constitutive equation for an incompressible Bingham fluid, the variational inequality and an operator-splitting numerical method for the solution of isothermal flow problems. Santos et al. [50] studied flow of viscoplastic fluids in a lid-driven cavity numerically as the viscoplastic material behavior was described by the model introduced by de Souza Mendes and Dutra. The influence of inertia and rheological parameters on the morphology of the material yield surfaces was analyzed and discussed. Syrakos et al. [51] investigated the capabilities and limitations of the popular finite volume/SIMPLE method coupled with the Papanastasiou regularization, by applying it to the simulation of Bingham flow in a lid driven cavity.

### *1.5 Viscoplastic fluids on natural convection in a cavity*

Natural convection of viscoplastic fluids in an enclosure has been considered during the last decade by researchers. Turan et al. [52] conducted a study into the simulations of natural convection in square enclosures filled with an incompressible Bingham fluid. The considered flow was laminar and steady. The commercial package FLUENT was utilised to solve the problem. In this study, a second-order central differencing scheme was used for the diffusive terms and a second order up-wind scheme for the convective terms. Coupling of the pressure and velocity fields was achieved using the SIMPLE algorithm. It should be noted that the default Bingham model in FLUENT is a bi viscosity model. Turan et al. [53] continued their studies with analysing the effect of different aspect ratios (the ratio of the height to the length) of the cavity, adding to their previous results that the average Nusselt number follows a non-monotonic pattern with the aspect ratio for specific values of the Rayleigh and Prandtl numbers for both Newtonian and Bingham fluids. At small aspect ratios, the conduction is dominant whereas convection remains predominantly responsible for the heat transfer for large values of aspect ratios. In addition, it was found that the conduction dominated regime occurred at higher values of the Bingham numbers for increasing values of the aspect ratio for a given value of the Rayleigh number. Turan et al. [54] scrutinised the laminar Rayleigh-Bnard convection of yield stress fluids in a square enclosure. The applied method and the achieved results were similar to the two previous studies. Huilgol and Kefayati [55] studied natural convection in a square cavity with differentially heated vertical sides and filled with a Bingham fluid

without any regularisation. The finite element method (FEM) based on the operator splitting method was utilised to solve the problem. It was observed that for specific Rayleigh and Prandtl numbers, the increase in the Bingham number decreases the heat transfer. Furthermore, it was found that the growth of the Bingham number expands the unyielded sections in the cavity. Finally, they mentioned that for fixed Rayleigh and Bingham numbers, the unyielded regions grow with the augmentation of the Prandtl number. Karimfazli et al. [56] explored the feasibility of a novel method for the regulation of heat transfer across a cavity. They used computational simulations to resolve the Navier-Stokes and energy equations for different yield stresses. Baranwal and Chhabra [57] studied laminar natural convection heat transfer to Bingham plastic fluids from two differentially heated isothermal cylinders confined in a square enclosure. They utilized regularization approaches of biviscosity and the Bercovier and Engelman models. They used the finite element method-based solver, COMSOL Multiphysics (version 4.3a) to solve the governing equations. Dutta et al. [58] investigated the effects of tilt angle and fluid yield stress on the laminar natural convection from an isothermal square bar cylinder in a Bingham plastic fluid confined in a square duct. They also applied the same regularization approaches of biviscosity and the Bercovier and Engelman models. They also applied the finite element method-based solver, COMSOL Multiphysics (version 4.3a) to solve the governing equations. Kefayati [59] simulated double-diffusive natural convection, studying Soret and Dufour effects and viscous dissipation in a square cavity filled with Bingham fluid by Finite Difference Lattice Boltzmann Method (FDLBM). In addition, entropy generations through fluid friction, heat transfer, and mass transfer were studied. The problem was solved by applying the regularised Papanastasiou model. Kefayati and Tang [60] studied double-diffusive natural convection of viscoplastic fluids in an open cavity by Lattice Boltzmann Method. In addition, entropy generations through fluid friction, heat transfer, and mass transfer were studied. The problem was solved by applying the regularised Papanastasiou model and the exact Bingham model. Kefayati and Tang [61–63] simulated natural convection in an inclined heated cavity with inner cold circular/elliptical cylinders filled with viscoplastic fluids by Lattice Boltzmann Method (LBM) in three parts (Part I: one cylinder, Part II: two cylinders, Part III: four cylinders). In this study, the Bingham model without any regularization was studied and moreover viscous dissipation effect also was analyzed. Fluid flow, heat transfer, and yielded/unyielded parts were conducted for certain pertinent parameters.

### *1.6 Viscoplastic fluids on mixed convection*

Mukherjee et al. [64] investigated the effects of the power-law and Bingham plastic viscosity on the flow and heat transfer characteristics of laminar forced convection through non-circular ducts of a range of cross-sections numerically

over the wide ranges of Peclet number, and Bingham number. Gupta and Chhabra [65] studied laminar mixed convection from an isothermal spheroidal particle immersed in a Bingham plastic fluid numerically in the buoyancy-assisted regime. The results reported over the wide ranges of Reynolds number, Prandtl number, Bingham number, Richardson number, and aspect ratio of the spheroid. Raja et al. [66] investigated the steady flow of a Bingham plastic fluid past a two-dimensional heated flat plate. The governing partial differential equations (continuity, momentum and thermal energy) were solved numerically over the range of conditions. Kefayati and Huilgol [67] utilized the mesoscopic method to conduct a two-dimensional simulation of steady mixed convection in a square enclosure with differentially heated sidewalls when the enclosure is filled with a Bingham fluid. The problem was solved by the Bingham model without any regularisations and also by applying the regularised Papanatasiou model.

### *1.7 The applied Numerical method*

Lattice Boltzmann method (LBM) has been demonstrated to be a very effective mesoscopic numerical method to model a broad variety of complex fluid flow phenomena [68–76]. This is because the main equation of the LBM is hyperbolic and can be solved locally, explicitly, and efficiently on parallel computers. However, the specific relation between the relaxation time and the viscosity has caused LBM not to have the considerable success in non-Newtonian fluid especially on energy equations. In this connection, Fu et al. [77] proposed a new equation for the equilibrium distribution function, modifying the LB model. Here, this equilibrium distribution function is altered in different directions and nodes while the relaxation time is fixed. Independency of the method to the relaxation time in contrast with common LBM provokes the method to solve different non-Newtonian fluid energy equations successfully as the method protects the positive points of LBM simultaneously. In addition, the validation of the method and its mesh independency demonstrates that is more capable than conventional LBM. Huilgol and Kefayati [78] explained and derived the two and three dimensional equations of continuum mechanics for this method and demonstrated that the theoretical development can be applied to all fluids, whether they be Newtonian, or power law fluids, or viscoelastic and viscoplastic fluids. Following the previous study, Huilgol and Kefayati [79] derived the two and three dimensional equations of this method for the cylindrical and spherical coordinates. Validation results obtained through the modelling of a mixed convection flow of a Bingham fluid in a lid-driven square cavity, and the steady flow of a Bingham fluid in a pipe of square cross-section. Next, using the cylindrical coordinate version of the evolution equations, numerical modelling of the steady flow of a Bingham fluid and the Herschel–Bulkley fluid in a pipe of circular cross-



section have been performed and compared with the simulation results using the augmented Lagrangian method as well as the analytical solutions for the velocity field and the flow rate. Kefayati and Huilgol [80] applied this method to simulate the steady flow in a pipe of square cross-section when the pipe was filled with a Bingham fluid. The problem was solved employing the Bingham model without any regularisation.

### 1.8 *The objectives*

The main aim of this study is to simulate laminar Magnetohydrodynamic (MHD) mixed convection of viscoplastic fluids in a lid-driven cavity with different aspect ratios as the yielded/unyielded sections have been displayed. In this study, the viscoplastic fluid has been analysed by the Bingham model without any regularization. Lattice Boltzmann method (LBM) has been employed to study the problem numerically and therefore the study is also interesting numerically. So, it is endeavoured to express the effects of different parameters (Rayleigh number, Aspect ratio, Reynolds number, Bingham number, Eckert number, Hartmann number, Joule heating parameter) on heat transfer, fluid flow as well as yielded/unyielded zones are studied.

## 2 **Theoretical formulation**

### 2.1 *Definition of the problem*

The geometry of the present problem is shown in figure 1. It consists of a two-dimensional cavity with the height  $H$  and the width  $L$ . For the present case, aspect ratio (AR) is defined as the ratio of the height to the width ( $AR = H/L$ ). The temperature of the left wall is maintained at a higher temperature than the right wall. The horizontal walls are adiabatic and impermeable and the top wall is driven from the left to right at a constant speed  $U_0$ . The cavity is filled with a viscoplastic fluid. The fluid flow is incompressible, laminar, and steady. The Grashof and Prandtl numbers are kept at  $Gr = 10^4$  and  $Pr = 1$ . The density variation is approximated by the standard Boussinesq model. A uniform magnetic field with a constant magnitude is applied in different inclinations ( $\theta$ ) where the horizontal direction from the left to right sides is the inclined angle of  $\theta = 0^\circ$ . For most industrial flows involving viscoplastic fluids e.g. liquid metal, magnetic Reynolds number is very low, usually less than  $10^{-2}$ . When an external magnetic field is present, it is customary at such low values of magnetic Reynolds number to make use an approximation.

In this approximation, induced magnetic fluctuations are much smaller than the applied magnetic field [81,82]. Therefore, the induced magnetic field is neglected. Moreover, Hall effect is assumed negligible.

## 2.2 MHD equations

As an electrically-conducting fluid moves with velocity  $\mathbf{u}$  through an imposed magnetic field, their average motion gives rise to an electric current density. The applied magnetic effect is the inclusion of the Lorentz body force to the momentum equations as follows [16–18,10,19–29]

$$\mathbf{F}_m = \mathbf{J} \times \mathbf{B} \quad (2.1)$$

According to Ohm's law, the electric current density  $\mathbf{J}$  is as

$$\mathbf{J} = \sigma (\mathbf{E} + \mathbf{u} \times \mathbf{B}) \quad (2.2)$$

$\sigma$  and  $\mathbf{E}$  are the electrical conductivity of the fluid and the electric field strength; respectively.

Due to the uniform magnetic field flux, the irrotational electric field is formed inside the enclosure.

$$\nabla \times \mathbf{B} = 0 \quad (2.3)$$

The electric field  $\mathbf{E}$  can be expressed as the gradient of electrical potential  $\Phi$  as follows:

$$\mathbf{E} = -\nabla\Phi \quad (2.4)$$

The conservation of electric current  $\mathbf{J}$  yields

$$\nabla \cdot \mathbf{J} = 0 \quad (2.5)$$

So, from the Eq.2.2 we have

$$\nabla^2\Phi = \nabla \cdot (\mathbf{u} \times \mathbf{B}) \quad (2.6)$$

For a two-dimensional MHD flow, it is shown that

$$\nabla \cdot (\mathbf{u} \times \mathbf{B}) = 0 \quad (2.7)$$

As a result

$$\nabla^2 \Phi = 0 \quad (2.8)$$

All walls of the enclosure are electrically insulated and the viscous no-slip boundary condition is applied on. In other words, the fluid is bounded by perfectly conducting walls that provide a resistance-free path from induced current. It follows that

$$\nabla \Phi = 0 \quad (2.9)$$

and therefore the electric field vanishes everywhere in the cavity. Finally, the Lorentz force by the induced current and the magnetic field flux can be calculated without solving the electromagnetism inside the cavity, as follows:

$$\mathbf{F}_m = \sigma (\mathbf{u} \times \mathbf{B}) \times \mathbf{B} \quad (2.10)$$

A uniform magnetic field of  $\mathbf{B} = B_x \mathbf{i} + B_y \mathbf{j}$  is imposed and it makes an angle of  $\theta$  with the horizontal axis. The magnitude of the magnetic field and the angle are

$$B = \sqrt{B_x^2 + B_y^2} \quad \theta = \tan^{-1} \left( \frac{B_x}{B_y} \right) \quad (2.11)$$

### 2.3 Dimensional equations

Based on the above assumptions, denoting by  $\mathbf{u} = u\mathbf{i} + v\mathbf{j}$  the velocity field,  $\rho$  the density, and  $T$  the temperature field, and applying the Boussinesq approximation, mass, momentum, and energy equations for the steady incompressible flow are:

$$\frac{\partial u}{\partial x} + \frac{\partial v}{\partial y} = 0, \quad (2.12)$$

$$\rho \left( \frac{\partial u}{\partial t} + u \frac{\partial u}{\partial x} + v \frac{\partial u}{\partial y} \right) = -\frac{\partial p}{\partial x} + \frac{\partial \tau_{xx}}{\partial x} + \frac{\partial \tau_{xy}}{\partial y} + \sigma B^2 (v \sin \theta \cos \theta - u \sin^2 \theta), \quad (2.13)$$

$$\rho \left( \frac{\partial v}{\partial t} + u \frac{\partial v}{\partial x} + v \frac{\partial v}{\partial y} \right) = -\frac{\partial p}{\partial y} + \frac{\partial \tau_{xy}}{\partial x} + \frac{\partial \tau_{yy}}{\partial y} + \rho g [1 + \beta (T - T_C)] + \sigma B^2 (u \sin \theta \cos \theta - v \cos^2 \theta), \quad (2.14)$$

Now, let the pressure  $p$  be written as the sum  $p = p_s + p_d$ , where the static part  $p_s$  accounts for gravity alone, and  $p_d$  is the dynamic part. Thus,

$$-\frac{\partial p_s}{\partial y} = \rho g. \quad (2.15)$$

where  $\beta$  is the coefficient of thermal expansion with the dimension of  $1/T$ , where  $T$  is the absolute temperature.  $\sigma$  is the electrical conductivity and  $B$  is the intensity of the external magnetic field. In addition,  $\theta$  is the angle of the external magnetic field with the horizontal direction counterclockwise.

$$\frac{\partial T}{\partial t} + u \frac{\partial T}{\partial x} + v \frac{\partial T}{\partial y} = \alpha \left( \frac{\partial^2 T}{\partial x^2} + \frac{\partial^2 T}{\partial y^2} \right) + \frac{1}{\rho c_p} \left[ \tau_{xx} \left( \frac{\partial u}{\partial x} \right) + \tau_{xy} \left( \frac{\partial u}{\partial y} + \frac{\partial v}{\partial x} \right) + \tau_{yy} \left( \frac{\partial v}{\partial y} \right) \right] + \frac{\sigma B^2}{\rho c_p} (u \sin \theta - v \cos \theta)^2, \quad (2.16)$$

$\alpha$  and  $c_p$  are the thermal diffusivity and the specific heat at constant pressure, respectively. It should be mentioned that the second and third terms in the right side of Eq.(2.16) are the viscous dissipation and joule heating terms; respectively. In addition,  $\tau_{xx}, \tau_{xy}, \tau_{yy}$  are the stresses of the stress tensor  $\boldsymbol{\tau}$ .

#### 2.4 Constitutive model

Bingham [83] constituted the viscoplastic fluids as follows:

$$\begin{cases} \mathbf{A}(\mathbf{u}) = \mathbf{0}, & K(\boldsymbol{\tau}) \leq \tau_y, \\ \boldsymbol{\tau} = \left( \eta + \frac{\tau_y}{K(\mathbf{u})} \right) \mathbf{A}(\mathbf{u}), & K(\boldsymbol{\tau}) > \tau_y, \end{cases} \quad (2.17)$$

where the viscosity  $\eta$  and the yield stress  $\tau_y$  are constant, and the two invariants  $K(\mathbf{u})$  and  $K(\boldsymbol{\tau})$  are defined below:

$$2K^2(\mathbf{u}) = \mathbf{A}(\mathbf{u}) : \mathbf{A}(\mathbf{u}), \quad 2K^2(\boldsymbol{\tau}) = \boldsymbol{\tau} : \boldsymbol{\tau}. \quad (2.18)$$

where

$$\mathbf{A}(\mathbf{u}) = \nabla \mathbf{u} + \nabla \mathbf{u}^T. \quad (2.19)$$

Due to the discontinuity in the Bingham model, approximate models such as the Papanastasiou [84], Bercovier and Engelman [85], and the bi-viscosity [86] models are used by researchers and different software packages. However, a constitutive equation for a Bingham fluid fully equivalent to the original form can be used. This method was proposed and developed by Duvaut and Lions [87] and Glowinski [88] and the constitutive equation takes the form

$$\boldsymbol{\tau} = \eta \mathbf{A}(\mathbf{u}) + \sqrt{2} \tau_y \boldsymbol{\Lambda}, \quad \mathbf{1} : \boldsymbol{\Lambda} = 0, \quad (2.20)$$

where one may call the second order, symmetric, tensor  $\boldsymbol{\Lambda}$  the *viscoplasticity constraint tensor*. Note that the traceless condition  $\mathbf{1} : \boldsymbol{\Lambda} = 0$  has been imposed on this tensor so that the stress tensor  $\boldsymbol{\tau}$  satisfies the condition  $\text{tr } \boldsymbol{\tau} = 0$ . In order to demarcate the flow field into unyielded/yielded zones, one requires that the tensor  $\boldsymbol{\Lambda}$  meet the following conditions:

$$\boldsymbol{\Lambda} : \boldsymbol{\Lambda} = \begin{cases} < 1, & \mathbf{A}(\mathbf{u}) = \mathbf{0}, \\ 1, & \mathbf{A}(\mathbf{u}) \neq \mathbf{0}. \end{cases} \quad (2.21)$$

These conditions satisfy those imposed on the stress tensor, viz.,  $K(\boldsymbol{\tau}) \leq \tau_y$  when  $\mathbf{A}(\mathbf{u}) = \mathbf{0}$ , and  $\tau_y < K(\boldsymbol{\tau})$  when  $\mathbf{A}(\mathbf{u}) \neq \mathbf{0}$ . The problem of determining where the flow is rigid and where it is liquid-like has been shifted to finding the tensor  $\boldsymbol{\Lambda}$  in the flow field such that it satisfies Eq.(2.21). What has been proposed is important for the following reasons:

- (1) The constitutive equations Eqs. (2.20) - (2.21) are defined over the entire flow domain, not just where the fluid has yielded.
- (2) One searches for the solution velocity field  $\mathbf{u}$  and the viscoplasticity constraint tensor  $\boldsymbol{\Lambda}$  to determine the yielded/unyielded regions. There are no singularities because one is not trying to find the location of the yield surface(s) through the limit of  $\mathbf{A}(\mathbf{u})/K(\mathbf{u})$  as  $\mathbf{A}(\mathbf{u}) \rightarrow \mathbf{0}$ .
- (3) However, the equations of motion now involve two unknown fields: a vector field  $\mathbf{u}$ , and a symmetric tensor field  $\boldsymbol{\Lambda}$ . The latter requires that there should exist a connection between the velocity field  $\mathbf{u}$  and  $\boldsymbol{\Lambda}$ . Under Dirichlet boundary conditions, it is possible to prove such a relation. Here, we provide a summary of the results.

$\mathbf{\Lambda}$  can be obtained from a simple projection operation as follows [55,80,67]:

$$\mathbf{\Lambda} = P_{\mathcal{M}}\left(\mathbf{\Lambda} + r\tau_y\mathbf{A}(\mathbf{u})\right), \quad \forall r > 0, \quad (2.22)$$

where  $\mathcal{M} = \{\boldsymbol{\mu} | \boldsymbol{\mu} = (\mu_{ij})_{1 \leq i, j \leq 2} \in (L^2(\Omega))^4, \|\boldsymbol{\mu}\| \leq 1 \text{ a.e. on } \Omega\}$  and

$$P_{\mathcal{M}} : (L^2(\Omega))^4 \rightarrow \mathcal{M} \quad (2.23)$$

is the projection operator defined so that  $P_{\mathcal{M}}(\boldsymbol{\mu}) = \boldsymbol{\mu}$ , if  $\|\boldsymbol{\mu}\| \leq 1$ , and  $P_{\mathcal{M}}(\boldsymbol{\mu}) = \boldsymbol{\mu} / \|\boldsymbol{\mu}\|$  otherwise. Note that in the context of Eq. (2.22), the tensor  $\boldsymbol{\mu} = \mathbf{\Lambda} + r\tau_y\mathbf{A}(\mathbf{u})$  and it is symmetric. Further, the tensor  $\boldsymbol{\mu}$  must be dimensionless for  $\mathbf{\Lambda}$  is also dimensionless.

where  $r > 0$  is a real number to be specified. Successive iterations are performed till convergence is achieved to the desired level of accuracy. Note that the yield surface is the boundary between  $\|\mathbf{\Lambda}\| < 1$  and  $\|\mathbf{\Lambda}\| = 1$ . Hence, the solution of the boundary value problem delivers in the limit both the velocity field as well as the shape and location of the yield surface. For more information, see [55,67,80,89].

### 2.5 Dimensional boundary condition

The flow domain is given by  $\Omega = (0, L) \times (0, H)$ , and the boundary  $\Gamma = \partial\Omega$ . It is the union of four disjoint subsets:

$$\Gamma_1 = \{(x, y), x = 0, 0 \leq y \leq H\}, \quad \Gamma_2 = \{(x, y), x = L, 0 \leq y \leq H\} \quad (2.24)$$

$$\Gamma_3 = \{(x, y), 0 \leq x \leq L, y = 0\}, \quad \Gamma_4 = \{(x, y), 0 \leq x \leq L, y = H\}. \quad (2.25)$$

The boundary condition for the velocity is straightforward:

$$\mathbf{u}|_{\Gamma_1} = \mathbf{u}|_{\Gamma_2} = \mathbf{u}|_{\Gamma_3} = \mathbf{0}, \quad \mathbf{u}|_{\Gamma_4} = U_0\mathbf{i}. \quad (2.26)$$

The boundary conditions for the temperature are:

$$T|_{\Gamma_1} = T_H, \quad T|_{\Gamma_2} = T_C, \quad \partial T / \partial y|_{\Gamma_3} = 0, \quad \partial T / \partial y|_{\Gamma_4} = 0. \quad (2.27)$$

### 2.6 Non-dimensional equations

In order to proceed to the numerical solution of the system, the following non dimensional variables are introduced [59,60,67].

$$t^* = \frac{t U_0}{L}, \quad x^* = x/L, \quad y^* = y/L, \quad \mathbf{u}^* = \frac{\mathbf{u}}{U_0}, \quad p_d^* = \frac{p_d}{\rho U_0^2}, \quad (2.28)$$

$$T^* = (T - T_C)/\Delta T, \quad \Delta T = T_H - T_C, \quad \boldsymbol{\tau}^* = \frac{\boldsymbol{\tau} L}{\eta U_0} \quad (2.29)$$

where  $U_0$  is the speed of the upper wall.

By substitution of Eqs. (2.28) and (2.29) into Eqs. (2.12) - (2.16) and dropping the asterisks \* for convenience, the following system of non-dimensional equations is derived:

$$\frac{\partial u}{\partial x} + \frac{\partial v}{\partial y} = 0, \quad (2.30)$$

$$\frac{\partial u}{\partial t} + u \frac{\partial u}{\partial x} + v \frac{\partial u}{\partial y} = -\frac{\partial p_d}{\partial x} + \frac{1}{\text{Re}} \left( \frac{\partial \tau_{xx}}{\partial x} + \frac{\partial \tau_{xy}}{\partial y} \right) + \frac{\text{Ha}^2}{\text{Re}} \left( v \sin\theta \cos\theta - u \sin^2\theta \right), \quad (2.31)$$

$$\begin{aligned} \frac{\partial v}{\partial t} + u \frac{\partial v}{\partial x} + v \frac{\partial v}{\partial y} = -\frac{\partial p_d}{\partial y} + \frac{1}{\text{Re}} \left( \frac{\partial \tau_{xy}}{\partial x} + \frac{\partial \tau_{yy}}{\partial y} \right) + \frac{\text{Gr}}{\text{Re}^2} T \\ + \frac{\text{Ha}^2}{\text{Re}} \left( u \sin\theta \cos\theta - v \cos^2\theta \right), \end{aligned} \quad (2.32)$$

$$\begin{aligned} \frac{\partial T}{\partial t} + u \frac{\partial T}{\partial x} + v \frac{\partial T}{\partial y} = \frac{1}{\text{Re Pr}} \left( \frac{\partial^2 T}{\partial x^2} + \frac{\partial^2 T}{\partial y^2} \right) + \frac{\text{Ec}}{\text{Re}} \left[ \tau_{xx} \left( \frac{\partial u}{\partial x} \right) + \tau_{xy} \left( \frac{\partial u}{\partial y} + \frac{\partial v}{\partial x} \right) + \tau_{yy} \left( \frac{\partial v}{\partial y} \right) \right] \\ + \frac{\text{Ha}^2 \text{Ec}}{\text{Re}} (u \sin\theta - v \cos\theta)^2, \end{aligned} \quad (2.33)$$

In the case of the exact Bingham model (Huilgol [89]), the non-dimensional stresses are given by

$$\tau_{xx} = \left[ 2 \left( \frac{\partial u}{\partial x} \right) + \sqrt{2} \text{Bn} \Lambda_{xx} \right], \quad (2.34a)$$

$$\tau_{yy} = \left[ 2 \left( \frac{\partial v}{\partial y} \right) + \sqrt{2} \text{Bn} \Lambda_{yy} \right], \quad (2.34b)$$

$$\tau_{xy} = \left[ \left( \frac{\partial u}{\partial y} + \frac{\partial v}{\partial x} \right) + \sqrt{2} \text{Bn} \Lambda_{xy} \right], \quad (2.34c)$$

$$\mathbf{\Lambda}^{n+1} = P_{\mathcal{M}} \left( \mathbf{\Lambda}^n + \text{PrBn} \mathbf{A}_1^n \right). \quad (2.35)$$

The non-dimensional parameters for the problem are as follows:

Grashof number:

$$\text{Gr} = \frac{\rho^2 \beta g L^3 \Delta T}{\eta^2}. \quad (2.36)$$

Prandtl number:

$$\text{Pr} = \frac{\eta}{\rho \alpha}, \quad (2.37)$$

Reynolds number:

$$\text{Re} = \frac{\rho U_0 L}{\eta}, \quad (2.38)$$

Bingham number:

$$\text{Bn} = \frac{\tau_y L}{\eta U_0}. \quad (2.39)$$

Hartmann number:

$$\text{Ha} = BL \sqrt{\sigma/\eta}, \quad (2.40)$$

Eckert number:

$$\text{Ec} = \frac{U_0^2}{c_p \Delta T} \quad (2.41)$$

Since the  $U_0$  and  $\Delta T$  are equal to unity, the Eckert number has an inverse proportion to the specific heat at constant pressure  $\text{Ec} \propto \frac{1}{c_p}$ . The  $c_p$  for different viscoplastic fluids in various temperatures can be ranged over  $10^2$  and  $10^4$  J/kg K. So, we studied the Eckert numbers of  $\text{Ec} = 0, 10^{-4}, 10^{-3}$ , and  $10^{-2}$  here. As the most viscoplastic materials in the cited ranges have  $c_p = 10^3$ , we have studied other parameters, e.g. Reynolds numbers, aspect ratios, Bingham numbers at constant Eckert number of  $\text{Ec} = 10^{-3}$ .



## 2.7 Non-dimensional boundary condition

The flow domain is given by  $\Omega = (0, 1) \times (0, \text{AR})$ , and the boundary  $\Gamma = \partial\Omega$ . It is the union of four disjoint subsets:

$$\Gamma_1 = \{(x, y), x = 0, 0 \leq y \leq \text{AR}\}, \quad \Gamma_2 = \{(x, y), x = 1, 0 \leq y \leq \text{AR}\} \quad (2.42)$$

$$\Gamma_3 = \{(x, y), 0 \leq x \leq 1, y = 0\}, \quad \Gamma_4 = \{(x, y), 0 \leq x \leq 1, y = \text{AR}\} \quad (2.43)$$

The boundary condition for the velocity is straightforward:

$$\mathbf{u}|_{\Gamma_1} = \mathbf{u}|_{\Gamma_2} = \mathbf{u}|_{\Gamma_3} = \mathbf{0}, \quad \mathbf{u}|_{\Gamma_4} = \mathbf{i}. \quad (2.44)$$

The boundary conditions for the temperature are:

$$T|_{\Gamma_1} = 1, \quad T|_{\Gamma_2} = 0, \quad \partial T / \partial y|_{\Gamma_3} = 0, \quad \partial T / \partial y|_{\Gamma_4} = 0. \quad (2.45)$$

## 3 The numerical method

The LBM equations and their relationships with continuum equations have been explained in details in Huilgol and Kefayati [78,79]. Here, just a brief description about the main equations would be cited. In addition, the applied algorithm has been described and the studied problem equations in the LBM are mentioned.

### 3.1 The Continuity and Momentum equations

To have the continuity and momentum equations, a discrete particle distribution function  $f_\alpha$  is defined over a D2Q9 lattice where it should satisfy an evolution equation:

$$\frac{\partial f_\alpha}{\partial t} + \boldsymbol{\xi}_\alpha \cdot \nabla_{\mathbf{x}} f_\alpha - F_\alpha = -\frac{1}{\varepsilon \phi} (f_\alpha - f_\alpha^{eq}), \quad (3.1)$$

where  $\varepsilon$  is a small parameter to be prescribed when numerical simulations are considered.  $\phi$  is the relaxation time and  $F_\alpha$  is the body force term.

Associated to each node is a lattice velocity vector  $\boldsymbol{\xi}_\alpha$ . It is defined as follows:

$$\boldsymbol{\xi}_\alpha = \begin{cases} (0, 0), & \alpha = 0, \\ c (\cos \Theta_\alpha, \sin \Theta_\alpha) & \alpha = 1, 3, 5, 7, \\ c \sqrt{2} (\cos \Theta_\alpha, \sin \Theta_\alpha), & \alpha = 2, 4, 6, 8. \end{cases} \quad (3.2)$$

Here, the angles  $\Theta_\alpha$  are defined through  $\Theta_\alpha = (\alpha - 1)\pi/4$ ,  $\alpha = 1, \dots, 8$ . The constant  $c$  has to be chosen with care for it affects numerical stability; its choice depends on the problem. The method for finding the parameter  $c$  which satisfies the Courant-Friedrichs-Lewy (CFL) condition is described in the Appendix.

The equilibrium distribution function,  $f_\alpha^{eq}$ , is different from the conventional ones adopted by previous researchers, who normally expand the Maxwellian distribution function. In the present approach, we expand  $f_\alpha^{eq}$  as a quadratic in terms of  $\boldsymbol{\xi}_\alpha$ , using the notation of linear algebra:

$$f_\alpha^{eq} = A_\alpha + \boldsymbol{\xi}_\alpha \cdot \mathbf{B}_\alpha + (\boldsymbol{\xi}_\alpha \otimes \boldsymbol{\xi}_\alpha) : \mathbf{C}_\alpha, \quad \alpha = 0, 1, 2, \dots, 8. \quad (3.3)$$

Here, the scalars  $A_\alpha$  are defined through

$$A_0 = \rho - \frac{2p}{c^2} - \frac{\rho|\mathbf{u}|^2}{c^2}, \quad A_\alpha = 0, \quad \alpha = 1, 2, \dots, 8. \quad (3.4)$$

The vectors  $\mathbf{B}_\alpha$  are given by

$$\mathbf{B}_1 = \frac{\rho\mathbf{u}}{2c^2} = \mathbf{B}_\alpha, \quad \alpha = 1, 3, 5, 7; \quad \mathbf{B}_\alpha = \mathbf{0}, \quad \alpha = 0, 2, 4, 6, 8. \quad (3.5)$$

Next, the matrices  $\mathbf{C}_\alpha$  are such that  $\mathbf{C}_0 = \mathbf{0}$ ;  $\mathbf{C}_1 = \mathbf{C}_\alpha$ ,  $\alpha = 1, 3, 5, 7$ ;  $\mathbf{C}_2 = \mathbf{C}_\alpha$ ,  $\alpha = 2, 4, 6, 8$ , where

$$\mathbf{C}_1 = \begin{bmatrix} C_{11} & 0 \\ 0 & C_{22} \end{bmatrix}, \quad C_{11} = \frac{1}{2c^4}(p + \rho u^2 - \frac{1}{\text{Re}} \tau_{xx}), \quad C_{22} = \frac{1}{2c^4}(p + \rho v^2 - \frac{1}{\text{Re}} \tau_{yy}), \quad (3.6)$$

$$\mathbf{C}_2 = \begin{bmatrix} 0 & C_{12} \\ C_{21} & 0 \end{bmatrix}, \quad C_{12} = C_{21} = \frac{1}{8c^4}(\rho uv - \frac{1}{\text{Re}} \tau_{xy}). \quad (3.7)$$

The body force term  $F_\alpha$  in (3.1) can be defined as

$$F_\alpha = 0, \quad \alpha = 0, 2, 4, 6, 8, \quad (3.8a)$$

$$F_\alpha = \frac{1}{2c^2} \mathbf{N} \cdot \boldsymbol{\xi}_\alpha, \quad \alpha = 1, 3, 5, 7 \quad (3.8b)$$

where

$$\mathbf{N} = \frac{\text{Gr}}{\text{Re}^2} T + \frac{\text{Ha}^2}{\text{Re}} \left[ \left( v \sin\theta \cos\theta - u \sin^2\theta \right) \mathbf{i} + \left( u \sin\theta \cos\theta - v \cos^2\theta \right) \mathbf{j} \right] \quad (3.9)$$

It should be noted that the macroscopic variables  $(u, v, T, p)$ ; here, are non-dimensional.

The main equations of the discrete particle distribution function (3.1) is solved by the splitting method of Toro [90]. Hence, the equations can be separated into two parts. The first one is the streaming section which is written as

$$\frac{\partial f_\alpha}{\partial t} + \boldsymbol{\xi}_\alpha \cdot \nabla_{\mathbf{x}} f_\alpha - F_\alpha = 0. \quad (3.10)$$

Eqs.(3.10) has been solved with the method of Lax and Wendroff [91] and the following equations are used.

$$\begin{aligned} f_\alpha^{n+1}(i, j) = & f_\alpha^n(i, j) - \frac{\Delta t}{2\Delta x} \xi_\alpha(i) [f_\alpha^n(i+1, j) - f_\alpha^n(i-1, j)] \\ & - \frac{\Delta t}{2\Delta y} \xi_\alpha(j) [f_\alpha^n(i, j+1) - f_\alpha^n(i, j-1)] + \\ & \frac{\Delta t^2}{2\Delta x^2} \xi_\alpha^2(i) [f_\alpha^n(i+1, j) - 2f_\alpha^n(i, j) + f_\alpha^n(i-1, j)] + F_\alpha(i)\Delta t + \\ & \frac{\Delta t^2}{2\Delta y^2} \xi_\alpha^2(j) [f_\alpha^n(i, j+1) - 2f_\alpha^n(i, j) + f_\alpha^n(i, j-1)] + F_\alpha(j)\Delta t, \quad (3.11) \end{aligned}$$

$\Delta x$  and  $\Delta y$  are lattice spacing in x and y directions; respectively.  $\Delta t$  is the time increment.

In Eqs.(3.11), we have put

$$\xi_\alpha(i) = \boldsymbol{\xi}_\alpha \cdot \mathbf{i}, \quad \xi_\alpha(j) = \boldsymbol{\xi}_\alpha \cdot \mathbf{j}, \quad F_\alpha(i) = \mathbf{F}_\alpha \cdot \mathbf{i}, \quad F_\alpha(j) = \mathbf{F}_\alpha \cdot \mathbf{j}. \quad (3.12)$$

The second part is the collision section which is as follows:

$$\frac{\partial f_\alpha}{\partial t} = -\frac{1}{\varepsilon\phi}(f_\alpha(\mathbf{x}, t) - f_\alpha^{eq}(\mathbf{x}, t)), \quad (3.13)$$

Eqs.(3.13) can be solved by using the Euler method and the choice of  $\varepsilon\phi$  is taken as the time step ( $\Delta t$ ). That is

$$\frac{f_\alpha(\mathbf{x}, t + \Delta t) - f_\alpha(\mathbf{x}, t)}{\Delta t} = -\frac{1}{\varepsilon\phi}(f_\alpha(\mathbf{x}, t) - f_\alpha^{eq}(\mathbf{x}, t)), \quad (3.14)$$

from which one obtains

$$f_\alpha(\mathbf{x}, t + \Delta t) = f_\alpha^{eq}(\mathbf{x}, t), \quad (3.15)$$

### 3.2 The Energy Equation

In order to obtain the energy equation, an internal energy distribution function  $g_\alpha$  is introduced and it is assumed to satisfy an evolution equation similar to that for  $f_\alpha$ . Thus,

$$\frac{\partial g_\alpha}{\partial t} + \boldsymbol{\xi}_\alpha \cdot \nabla_{\mathbf{x}} g_\alpha - G_\alpha = -\frac{1}{\varepsilon\phi}(g_\alpha - g_\alpha^{eq}). \quad (3.16)$$

Here,  $g_\alpha^{eq}$  has a monomial expansion:

$$g_\alpha^{eq} = D_\alpha + \boldsymbol{\xi}_\alpha \cdot \mathbf{E}_\alpha, \quad (3.17)$$

One way of satisfying the above is to assume, as before, that the scalars are given by  $D_\alpha = D_1$ ,  $\alpha = 1, 3, 5, 7$ , and  $D_\alpha = D_2$ ,  $\alpha = 2, 4, 6, 8$ . In this problem, the non-dimensional parameters are obtained as follows:

$$D_0 = T, \quad D_1 = 0, \quad D_2 = 0. \quad (3.18)$$

Regarding the vectors, it is assumed that  $\mathbf{E}_0 = \mathbf{0}$ ,  $\mathbf{E}_\alpha = \mathbf{E}_1$ ,  $\alpha = 1, 3, 5, 7$ ;  $\mathbf{E}_\alpha = \mathbf{E}_2$ ,  $\alpha = 2, 4, 6, 8$ , where

$$\mathbf{E}_1 = \frac{\mathbf{u}T + \frac{E_c}{Re} [(u\tau_{xx} + v\tau_{xy}) + (u\tau_{yx} + v\tau_{yy})]}{2c^2}. \quad (3.19)$$

The parameter  $G_\alpha$  can be defined as (See Eqs.3.44–3.48 in Huilgol and Kefayati [78])

$$G_\alpha = 0, \quad \alpha = 0, 2, 4, 6, 8, \quad (3.20a)$$

$$G_\alpha = \frac{Ec}{Re} \frac{Ha^2}{Re} (u \sin \theta - v \cos \theta)^2, \quad \alpha = 1, 3, 5, 7 \quad (3.20b)$$

The main equations of the internal energy distribution function are solved by the splitting method of Toro [90]. Hence, the equations can be separated into two parts. The first one is the streaming section which is written as

$$\frac{\partial g_\alpha}{\partial t} + \boldsymbol{\xi}_\alpha \cdot \nabla_{\mathbf{x}} g_\alpha - G_\alpha = 0. \quad (3.21)$$

Eqs.(3.21) have been solved with the method of Lax and Wendroff [91] and the following equations are used.

$$\begin{aligned} g_\alpha^{n+1}(i, j) = & g_\alpha^n(i, j) - \frac{\Delta t}{2\Delta x} \xi_\alpha(i) [g_\alpha^n(i+1, j) - g_\alpha^n(i-1, j)] \\ & - \frac{\Delta t}{2\Delta y} \xi_\alpha(j) [g_\alpha^n(i, j+1) - g_\alpha^n(i, j-1)] + \\ & \frac{\Delta t^2}{2\Delta x^2} \xi_\alpha^2(i) [g_\alpha^n(i+1, j) - 2g_\alpha^n(i, j) + g_\alpha^n(i-1, j)] + G_\alpha(i)\Delta t + \\ & \frac{\Delta t^2}{2\Delta y^2} \xi_\alpha^2(j) [g_\alpha^n(i, j+1) - 2g_\alpha^n(i, j) + g_\alpha^n(i, j-1)] + G_\alpha(j)\Delta t \end{aligned} \quad (3.22)$$

The second part is the collision section which is as follows:

$$\frac{\partial g_\alpha}{\partial t} = -\frac{1}{\varepsilon\phi} (g_\alpha(\mathbf{x}, t) - g_\alpha^{eq}(\mathbf{x}, t)). \quad (3.23)$$

Eqs.(3.23) can be solved by using the Euler method and the choice of  $\varepsilon\phi$  is taken as the time step ( $\Delta t$ ). That is

$$\frac{g_\alpha(\mathbf{x}, t + \Delta t) - g_\alpha(\mathbf{x}, t)}{\Delta t} = -\frac{1}{\varepsilon\phi} (g_\alpha(\mathbf{x}, t) - g_\alpha^{eq}(\mathbf{x}, t)), \quad (3.24)$$

from which one obtains

$$g_\alpha(\mathbf{x}, t + \Delta t) = g_\alpha^{eq}(\mathbf{x}, t). \quad (3.25)$$

The local and the average Nusselt numbers at the hot wall with the utilization of the dimensionless parameters are obtained from

$$\text{Nu} = -\left(\frac{\partial T}{\partial x}\right)\bigg|_{x=0}, \quad (3.26)$$

$$\text{Nu}_{\text{avg}} = \frac{1}{AR} \int_0^{AR} \text{Nu} dy. \quad (3.27)$$

### 3.3 Boundary conditions

One of the main advantages of the current approach is that boundary conditions can be incorporated in a manner similar to macroscopic methods, in contrast with other methods utilised for solving LBM equations. The latter employ complicated special relationships for the discrete particle distribution function ( $f_\alpha$ ) and the internal energy distribution function ( $g_\alpha$ ) for each kind of boundary conditions and problems [96,97]. For example, methods such as on-grid and mid-grid bounce back are used when the velocity is zero on the boundary; when the boundary is in motion, bounce-back is used along with a set of linear equations to determine the boundary values  $f_\alpha$ . In the method used here, the boundary conditions of  $f_\alpha$  and  $g_\alpha$  can be obtained directly from the macroscopic values on the boundaries due to the relationships of the macroscopic values with  $f_\alpha$  and  $g_\alpha$ . As a result, in this method, boundary conditions, especially the Dirichlet conditions, can be included in various problems similar to macroscopic methods and no special equations for  $f_\alpha$  and  $g_\alpha$  are needed to incorporate the boundary conditions. Therefore, we apply the cited macroscopic values (velocities and temperatures) on the boundary conditions directly.

## 4 Results and discussion

### 4.1 Code validation and grid independence

Lattice Boltzmann Method (LBM) has been employed in the numerical simulation of mixed convection flow in a lid-driven cavity filled with a Bingham fluid in the presence of a magnetic field. This problem has been investigated at different Reynolds numbers of ( $\text{Re} = 100, 500$  and  $1000$ ), Bingham numbers ( $\text{Bn} = 0, 1, 5$  and  $10$ ), Hartmann numbers ( $\text{Ha} = 0, 2,$  and  $5$ ), the aspect ratio ( $\text{AR} = 0.25, 1,$  and  $4$ ), and Eckert number ( $\text{Ec} = 0, 10^{-4}, 10^{-3},$  and  $10^{-2}$ ),

while the Grashof and Prandtl numbers are fixed at  $Gr = 10^4$  and  $Pr = 1$ . To justify the accuracy of the selected ranges, please see the references [16–29,59–63]. Since, in higher Hartmann numbers than  $Ha = 5$  for high aspect ratios ( $AR = 4$ ), unyielded parts fill the entire enclosure, the Hartmann number is limited to  $Ha = 5$  in the studied cases. An extensive mesh testing procedure was conducted to guarantee a grid independent solution. Seven different mesh combinations were explored for the case of  $Re = 100$ ,  $Ha = 2$ ,  $Bn = 1$ ,  $Ec = 10^{-3}$ ,  $AR = 1$ , and  $\theta = 0^\circ$ . It was confirmed that the grid size (200\*200) ensured a grid independent solution as portrayed in Table 1. To demonstrate the accuracy of the present results, MHD mixed convection of power-law fluids and non-Newtonian nanofluids were studied, using this code by the present code. Kefayati [92,93] analyzed laminar mixed convection of non-Newtonian nanofluids in a square lid-driven cavity in the presence of a magnetic field in different boundary conditions by the present code. Kefayati [94,95] simulated the effect of a magnetic field on mixed convection of shear-thinning fluids in a square lid-driven cavity with various boundary conditions under the combined buoyancy effects of thermal and mass diffusion by the present code. To verify the accuracy of the code for mixed convection of Bingham, it should be noted that Kefayati and Huilgol [67] utilized the present code to conduct a two-dimensional simulation of steady mixed convection in a square enclosure with differentially heated sidewalls when the enclosure was filled with a Bingham fluid. The problem was solved by the Bingham model without any regularisations. In addition, we set the time step  $\Delta t = 0.0001$  for this calculation and based on the validations, the final (developed) stage was defined at the non-dimensional time  $t^* = 90$ . To see the process of convection and yielding before the final stage, Fig.2 presents the isotherms, streamlines, and yielded/unyielded zones at  $Re = 1000$ ,  $AR = 0.25$ ,  $Ec = 10^{-3}$ ,  $Bn = 1$ ,  $\theta = 0^\circ$ , and  $Ha = 2$  in different non-dimensional time ( $t^* = 5, 10, 20, 50, \text{ and } 90$ ). The running time for the selected grid (200\*200) and non-dimensional time ( $t^* = 90$ ) is 9283 seconds. The value of  $c$  in the numerical method was varied in each iteration according to the Appendix.

#### 4.2 *Effect of Hartmann number*

The figure 3 presents the isotherms for different Hartmann numbers and aspect ratios at  $Bn = 1$ ,  $\theta = 0^\circ$ ,  $Ec = 10^{-3}$ , and  $Re = 100$ . It is obvious that the gradient of temperature on the hot wall decreases generally as the aspect ratio grows. When the power of the magnetic field rises, the isotherms move across of the enclosures less than lower Hartmann numbers. This movement of the isotherms demonstrates that the convection process decrease where at  $AR = 4$  and  $Ha = 5$  the isotherm behave similar to a pure conduction.

The figure 4 illustrates the streamlines for different Hartmann numbers and

aspect ratios at  $Bn = 1$ ,  $\theta = 0^\circ$ ,  $Ec = 10^{-3}$ , and  $Re = 100$ . As Hartmann number increases from  $Ha = 0$  to 5, the main vortex in the cavity changes in the middle of cavity. It exhibits the movement of streamline diminishes inside of the cavity and confirms the convection process decreases significantly in various aspect ratios. The shapes of the streamlines in different aspect ratios demonstrate that the increase in the aspect ratio from  $AR = 0.25$  to 4 reduces the movement of the fluid flow substantially.

The figure 5 indicates the yielded and unyielded zones for different Hartmann numbers and aspect ratios at  $Bn = 1$ ,  $\theta = 0^\circ$ ,  $Ec = 10^{-3}$ , and  $Re = 100$ . It displays the change of aspect ratio causes the unyielded section to alter considerably. At  $Ha = 0$  and  $AR = 0.25$ , the majority of the unyielded part is generated in the middle of the cavity; although there are small sections of unyielded parts in different parts of the enclosure. For  $AR = 1$ , the majority of the unyielded part is created on the top left side of the enclosure. For  $AR = 4$ , the unyielded sections are produced close to side walls and their sizes are different from other aspect ratios. When Hartmann number increases from  $Ha = 0$  to 2, the shape, location and size of the unyielded part change in different aspect ratios. For  $AR = 0.25$ , the unyielded part expands significantly in the same position at  $Ha = 0$ . But, for  $AR = 1$ , the size of the unyielded section enhances marginally and the plastic part on the top left side moves to the bottom and top middle of the enclosure. For  $AR = 4$ , the unyielded regions close to the side wall in the absence of the magnetic field expand at  $Ha = 2$  and two solid sections in the middle of the cavity close to the top and bottom horizontal sides are generated. The rise of Hartmann number from  $Ha = 2$  to 5 does not alter the size of the unyielded part at  $AR = 0.25$  markedly. However, the unyielded sections augment considerably at  $AR = 1$  and 4. It demonstrates that the yielded parts on the bottom side of the cavity converts to unyielded material at  $AR = 1$  and  $Ha = 5$ . At  $AR = 4$ , the most parts of the cavity fills with the unyielded part and just there is small yielded sections on the top of the enclosure.

The figures 6 demonstrate the effect of the Hartmann number on the local Nusselt number on the hot wall, horizontal velocities in the middle of the cavity ( $x = 0.5$ ) as well as the temperature profile and vertical velocities at  $y = 0.5$  for  $Bn = 1$ ,  $\theta = 0^\circ$ ,  $Ec = 10^{-3}$ ,  $AR = 1$ , and  $Re = 100$ . It shows that the local Nusselt number at  $Y < 0.8$  declines gradually as Hartmann number increases. But, the local Nusselt number shows nearly the same pattern at  $Y > 0.8$ . It shows that the curved shape of temperature at  $Ha = 0$  alters to a linear one at  $Ha = 5$  which demonstrates the convection process drops considerably. The same behaviour is observed in the vertical velocity due to the rise of Hartmann number. In other words, the enhancement of magnetic field strength diminishes the vertical velocity magnitude steadily. The magnitude of the maximum horizontal velocity declines regularly as the Hartmann number increases. It also shows that position of the maximum horizontal velocity



moves from the  $Y = 0.4$  at  $Ha = 0$  to  $Y = 0.8$  at  $Ha = 5$ .

Table 2 shows the average Nusselt number on the hot wall for different Hartmann numbers at  $Bn = 1$ ,  $\theta = 0^\circ$ ,  $Ec = 10^{-3}$ , and  $Re = 100$ . It indicates that the increase in the aspect ratio enhances the average Nusselt number in various Hartmann numbers. In addition, the rise of Hartmann number in different aspect ratios decreases the average Nusselt number gradually.

### 4.3 Effect of Bingham number

The figure 7 presents the isotherms for different Bingham numbers and aspect ratios at  $Ha = 0$ ,  $Ec = 10^{-3}$ , and  $Re = 100$ . At  $Bn = 1$ , it is evident that the increase in the aspect ratio alters the shape of the isotherms significantly since the isotherms on the hot wall come together more and more. In fact, the drop of the gradient of isotherms on the hot wall in the fixed buoyant flow causes the cited pattern to be created. In other words, the trend demonstrates that the convection process has weakened with the increase in the aspect ratio. Increasing the Bingham number to  $Bn = 5$  affects the isotherms for various aspect ratios marginally, although the isotherms demonstrate that the heat transfer decreases slightly; this can be seen from the isotherms of  $T = 0.3$  and  $0.2$  evidently. However, the isotherms of the aspect ratio  $AR = 4$  are influenced significantly by the rise of Bingham number from  $Bn = 1$  to  $5$  compared to other aspect ratios. However, at  $Bn = 10$ , the increase in the Bingham number has caused the isotherm gradients on the hot wall to decline and as a result, the convection process is weakened. Obviously, as the Bingham number increases, conductive heat transfer dominates the region next to the hotter wall, while next to the cooler one, convective heat transfer occurs. However, the movement of the upper plate to the right means that convective heat transfer can never disappear totally, for any finite Bingham number. Although, the isotherms at  $AR = 4$  and  $Bn = 10$  behave similar to a pure conduction process since the isotherms are nearly parallel to the side walls of the cavity.

The figure 8 illustrates the streamlines for different Bingham numbers and aspect ratios at  $Ha = 0$ ,  $Ec = 10^{-3}$ , and  $Re = 100$ . For different Bingham numbers, clockwise circulations have occupied the cavity in different aspect ratios where the buoyancy effect alters as the Bingham number changes. For  $Bn = 1$ , the strength movement of the vortex due to the rise of the aspect ratio from  $AR = 0.25$  to  $4$  proves that the convection procedure has been intensified by the rise of the aspect ratio. In fact, the intensity of the inertia force compared to the forced convection causes the core of the main circulation to move to the middle of the cavity at  $AR = 4$  from the corner side at  $AR = 0.25$ . The inclination of the streamlines cores to the middle of the cavity

at  $Bn = 5$  confirms that natural convection has strengthened and the role of the forced flow has become weak. In addition, the streamlines on the bottom of the cavity moves slightly due to the generation of the unyielded section. The trend is followed at  $Bn = 10$  where the streamlines are removed on the bottom half of the cavity; notably at  $AR = 4$ . It is clear that the core of the main circulation becomes closer to the upper section and therefore it can be stated that the increase in the Bingham number decreases the free convection influence generally and ameliorates the forced flow effect.

The figure 9 indicates the yielded and unyielded zones for different Bingham numbers and aspect ratios at  $Ha = 0$ ,  $Ec = 10^{-3}$ , and  $Re = 100$ . It shows that the rise of the Bingham number for various aspect ratios enhances the unyielded zone steadily. As Bingham number increases from  $Bn = 1$  to 5, the unyielded sections expand considerably at  $AR = 0.25$  and 4. But, at  $AR = 1$ , more than the half of the cavity space belongs to yielded zones. In addition, at  $Bn = 5$ , the unyielded parts are concentrated in the middle of the cavity at  $AR = 0.25$ , and the bottom and left top side of the cavity at  $AR = 1$ . At  $Bn = 10$ , the majority of the cavity fills with the solid region for aspect ratios  $AR = 0.25$  and 4; however, the increment of the unyielded zones at  $AR = 1$  is less than  $AR = 0.25$  and 4.

The figures 10 demonstrate the effect of the Bingham number on the local Nusselt number on the hot wall, horizontal velocities in the middle of the cavity ( $x = 0.5$ ) as well as the temperature profile and vertical velocities at  $y = 0.5$  for  $Bn = 1$ ,  $Ec = 10^{-3}$ ,  $AR = 1$ , and  $Re = 100$ . As the Bingham number increases from  $Bn = 1$  to 5, the local Nusselt number drops at  $Y < 0.5$  as the decline of the local Nusselt number by the rise of Bingham number decreases gradually between  $0 < Y < 0.5$  where the local Nusselt numbers in Bingham numbers of  $Bn = 1$  and 5 are the same at  $Y = 0.5$ . The main reason of the trend is the generation of the unyielded part at  $Y < 0.5$  for  $Bn = 5$ . But, between  $0.6 < Y < 0.9$  the local Nusselt number at  $Bn = 5$  is higher than those values at  $Bn = 1$ . The rise of Bingham number from  $Bn = 5$  to 10 does not alter the local Nusselt number at  $Y < 0.5$  since the unyielded parts are present in this section and therefore the heat transfer does not change. It should be noted the maximum values of local Nusselt numbers are observed at  $Y = 0.2$ , 0.9, and 0.8 for  $Bn = 1$ , 5, and 10; respectively. It is noticeable that the vertical velocity in the middle of the cavity drops as the Bingham number increases. It indicates that the strength of the natural and forced convection forces becomes increasingly weak in comparison to the viscous flow resistance for increasing values of the Bingham number. Hence, the fluid movement becomes more sluggish and eventually it leads to a drop in convection with the rise of Bingham number. This statement is further supported by the dimensionless temperature profiles as they become smoother in the middle of the cavity with declining Bingham numbers. The decrease in the curvature of the temperature and velocity distributions demonstrates that

the convection process weakens as the Bingham number enhances. Another phenomenon which has the potential to distinguish the role the Bingham number plays in decreasing the convection transport is the horizontal velocity in the middle of the cavity. The horizontal velocity progressively becomes linear with the rise of the Bingham number as a result of the weakening of convective transport.

Table 3 demonstrates the average Nusselt number on the hot wall for different Bingham numbers and aspect ratios at  $Ha = 0$ ,  $Ec = 10^{-3}$ , and  $Re = 100$ . It demonstrates that the increase in Bingham number decreases the average Nusselt number for different aspect ratios gradually. Further, the rise of aspect ratio in different Bingham numbers decreases the average Nusselt number considerably.

#### 4.4 *Effect of the Reynolds number*

The figure 11 reveals the isotherms, streamlines, and yielded/unyielded parts for different Reynolds numbers at  $Bn = 1$ ,  $Ha = 2$ ,  $AR = 1$ ,  $Ec = 10^{-3}$ , and  $\theta = 0^\circ$ . It is evident that the increase in the Reynolds number alters the shape of the isotherms significantly since the isotherms on the hot wall come together more and more. In fact, the augmentation of the forced flow in the fixed buoyant flow causes the cited pattern to be created. In other words, the trend demonstrates that the convection process has strengthened with the increase in Reynolds number. However, it also shows that the effect of Reynolds number enhancement is more noteworthy from  $Re = 100$  to 500 while the changes are insignificant from  $Re = 500$  to 1000. The movement of the core circulation from the center at  $Re = 100$  to the top right corner at  $Re = 1000$  proves the forced convection compared to the natural one to enhance steadily. The unyielded zone enhance considerably; noticeably on the bottom of the cavity, as Reynold number increases from  $Re = 100$  to 500. It confirms that natural convection has weakened and the role of the forced flow has become significant. But, the rise of the Reynolds number from  $Re = 500$  to 1000, diminishes the unyielded part on the bottom side of the enclosure while a solid part in the top middle of the enclosure is generated.

Table 4 exhibits the average Nusselt number on the hot wall for different Reynolds numbers at  $Ha = 2$ ,  $Bn = 1$ ,  $\theta = 0^\circ$ , and  $Ec = 10^{-3}$ . It shows the average Nusselt number increases significantly as Reynolds number enhances in different aspect ratios. In addition, it is observable the average Nusselt number declines generally when the aspect ratio rises. However, the drop due to the aspect ratio does not follow the same ratio. It depicts that the increase in the aspect ratio from  $AR = 0.25$  to 1, decreases the average Nusselt number nearly by 550%, 500%, and 350% for  $Re = 100$ , 500, and 1000; respectively. The

rise of the aspect ratio from  $AR = 1$  to 4, reduces the average Nusselt number nearly by 200%, 150%, and 160% for  $Re = 100$ , 500, and 1000; respectively.

#### 4.5 *Effect of the inclination of the magnetic field*

The figure 12 presents the isotherms for different inclinations of the magnetic field and aspect ratios at  $Bn = 1$ ,  $Ha = 5$ ,  $Ec = 10^{-3}$ , and  $Re = 100$ . It demonstrates that the rise of the magnetic field angle alters the isotherms clearly; however, the change is not the same in various aspect ratios and angles. At  $AR = 0.25$ , it is evident that the increase in the magnetic field angle causes the gradient of the isotherm on the hot wall to decline significantly and the movement of the isotherm between the cold and hot walls to drop considerably. But at  $AR = 1$ , the enhancement of the magnetic field angle increases the movement of isotherms between the side walls slightly. At  $AR = 4$ , the parallel isotherms similar to a pure conduction at  $\theta = 0^\circ$  changes to curved manners of isotherms due to the rise of convection at  $\theta = 90^\circ$ .

The figure 13 illustrates the streamlines for different inclinations of the magnetic field and aspect ratios at  $Bn = 1$ ,  $Ha = 5$ ,  $Ec = 10^{-3}$ , and  $Re = 100$ . At  $AR = 0.25$ , the increase in the magnetic field angle provokes the core of the streamlines move from the center of the enclosure to the left side and the streamlines on the bottom of the cavity disappears gradually. It demonstrates that the convection process weakens when the magnetic field angle rises. But by contrast, the movement of the streamlines between the horizontal sides enhance markedly and the core of the streamline moves to the center of the enclosure gradually. The pattern clearly demonstrates the rise of the magnetic field angle improves the convection process. At  $AR = 4$ , the increase in the magnetic field angle changes the streamline utterly and the core of the streamline moves from the top of the enclosure to the center of the enclosure. It confirms that the movement of the fluid flow strengthens substantially and therefore the convection process augments.

The figure 14 displays the yielded/unyielded parts for different inclinations of the magnetic field and aspect ratios at  $Bn = 1$ ,  $Ha = 5$ ,  $Ec = 10^{-3}$ , and  $Re = 100$ . The increase in the magnetic field angle from  $\theta = 0^\circ$  to  $60^\circ$  enhances the unyielded part at  $AR = 0.25$ , but the unyielded section dropped considerably at  $AR = 1$  and 4. The rise of the the magnetic field angle from  $\theta = 0^\circ$  to  $90^\circ$  augments the unyielded section slightly at  $AR = 0.25$ . At  $AR = 1$ , the unyielded section develops in the center of the enclosure vastly, but the unyielded part in the bottom corners of the enclosure diminishes. In addition, at  $AR = 4$ , the unyielded zone disappears in the most parts of the enclosure and there are just two concentrated unyielded zone close to the side walls.

Table 5 indicates the average Nusselt number on the hot wall for different inclinations of the magnetic field and aspect ratios at  $Ha = 5$ ,  $Bn = 1$ ,  $Ec = 10^{-3}$ , and  $Re = 100$ . At  $AR = 0.25$ , the rise of the magnetic field angle decreases the average Nusselt number gradually. At  $AR = 1$ , the enhancement of the magnetic field angle increases the average Nusselt number from  $\theta = 0^\circ$  to  $60^\circ$  steadily, but drops slightly at  $\theta = 90^\circ$ . At  $AR = 4$ , the average Nusselt number declines as the magnetic field angle rises especially at  $\theta = 90^\circ$ .

#### 4.6 Effect of the Eckert number

The figure 15 presents the isotherms, streamlines, yielded/unyielded sections for different aspect ratios and Eckert numbers at  $Bn = 1$ ,  $Ha = 5$ ,  $\theta = 30^\circ$ , and  $Re = 100$  (The solid red line ( $Ec=0.01$ ), and the dashed green line ( $Ec = 10^{-4}$ )). It demonstrates that the increase in the Eckert number does not change the isotherms, streamlines, and yielded/unyielded zones noticeably. However, it should be noted that there is a more visible alteration due to the Eckert number effect at  $AR = 0.25$  compared to other aspect ratios.

Table 6 demonstrates that the average Nusselt number on the hot wall for different Eckert numbers and aspect ratios at  $Ha = 5$ ,  $Bn = 1$ ,  $\theta = 30^\circ$ , and  $Re = 100$ . It indicates that the average Nusselt number declines marginally as the Eckert number increases in different aspect ratios. However, the average Nusselt number is influenced by the rise of Eckert number at  $AR = 0.25$  more than other aspect ratios.

## 5 Concluding Remarks

The mixed convection of viscoplastic fluids in a lid-driven cavity with different aspect ratios in the presence of a magnetic field has been analysed by Lattice Boltzmann method (LBM). The present study has been conducted with the main parameters in the following ranges: the Reynolds number ( $Re = 100, 500$ , and  $1000$ ), the Hartmann number ( $Ha = 0, 1, 2$ , and  $5$ ), the Bingham number ( $Bn = 1, 5$ , and  $10$ ), the aspect ratio ( $AR = 0.25, 1$ , and  $4$ ), the inclination of the magnetic field ( $\theta = 0^\circ, 30^\circ, 60^\circ$  and  $90^\circ$ ), and Eckert number ( $Ec = 0, 10^{-4}, 10^{-3}$ , and  $10^{-2}$ ) while the Grashof and Prandtl numbers are fixed at  $Gr = 10^4$  and  $Pr = 1$ ; respectively. This investigation is performed for various values of the mentioned parameters and the conclusions are summarised as follows:

- The enhancement of the Reynolds number increases the heat transfer for different aspect ratios, Hartmann numbers, and Bingham numbers and causes

the yielded/unyielded sections to alter.

- The rise of the aspect ratio decreases the heat transfer while augments the yielded/unyielded zones.
- The positions of the unyielded regions change in different aspect ratios.
- The increase in Hartmann number enlarges the unyielded sections and decreases the heat transfer in various aspect ratios and Reynolds numbers.
- The augmentation of the Bingham number reduces the heat transfer and increases the unyielded section in the cavity in different aspect ratios and Hartmann numbers.
- The rise of the aspect ratio increases the effect of the Hartmann number on the heat transfer and the unyielded part.
- The increase in the magnetic field angle from  $\theta = 0^\circ$  to  $90^\circ$  at  $AR = 0.25$  decreases the heat transfer and increases the unyielded region considerably.
- The rise of the magnetic field angle from  $\theta = 0^\circ$  to  $90^\circ$  at  $AR = 4$  enhances the heat transfer and diminishes the unyielded region significantly.
- The enhancement of the magnetic field angle from  $\theta = 0^\circ$  to  $90^\circ$  at  $AR = 1$  alters the heat transfer and the yielded/unyielded parts.
- The Eckert number in the studied range based on practical values has insignificant influences on heat transfer and yielded/unyielded parts in various aspect ratios.
- In the studied marginal effect of Eckert number, the drop of heat transfer at  $AR = 0.25$  are more than  $AR = 1$  and  $4$ .

## Acknowledgements

The first author(Gholamreza Kefayati (GH. R. Kefayati)) gratefully acknowledges the funding support in the form of a Research Fellowship awarded him by the Hong Kong Polytechnic University.

## Appendix

Here, we shall discuss the stability of the numerical scheme. Finding the parameter  $c$ , we multiply  $f_\alpha^{eq}$  with  $|\boldsymbol{\xi}_\alpha|^2/2$  and take the sum, which leads to

$$\sum_{\alpha=0}^8 \frac{1}{2} f_\alpha^{eq} |\boldsymbol{\xi}_\alpha|^2 = p + \frac{1}{2} \rho |\mathbf{u}|^2 - \frac{\tau_{xx} + \tau_{yy}}{2}. \quad (\text{A1})$$

Next, it is easy to verify that

$$\sum_{\alpha=0}^8 F_\alpha |\boldsymbol{\xi}_\alpha|^2 = 0. \quad (\text{A2})$$

Hence,

$$\frac{\partial}{\partial t} \left[ p + \frac{1}{2} \rho |\mathbf{u}|^2 - \frac{\tau_{xx} + \tau_{yy}}{2} \right] + \frac{c^2}{2} \rho (\nabla \cdot \mathbf{u}) = O(\varepsilon). \quad (\text{A3})$$

The Courant-Friedrichs-Lewy (CFL) condition states that [98,99]

$$K = \frac{u \Delta t}{\Delta x} + \frac{v \Delta t}{\Delta y} \leq 1. \quad (\text{A4})$$

This can be used in (A3) and we obtain

$$\left[ |\mathbf{u}|^2 + \frac{2p - \tau_{xx} - \tau_{yy}}{\rho} \right] + c^2 K = O(\varepsilon). \quad (\text{A5})$$

Thus, the lattice speed  $c$  must satisfy

$$c = K_c \sqrt{\left| \frac{\tau_{xx} + \tau_{yy} - 2p}{\rho} - |\mathbf{u}|^2 \right|}, \quad K_c = \frac{1}{\sqrt{K}} \geq 1. \quad (\text{A6})$$

Since the pressure  $p$  has to be uniquely defined in a Bingham fluid, one requires that  $\tau_{xx} + \tau_{yy} = 0$ ; . Thus, reduces to

$$c = K_c \sqrt{\left| \frac{-2p}{\rho} - |\mathbf{u}|^2 \right|}, \quad K_c = \frac{1}{\sqrt{K}} \geq 1 \quad (\text{A7})$$

As a result, the value  $c$  is modified and changes in each iteration as defined through (A7).

## References

- [1] J. Boguszynska, M. Brown, P. McDonald, J. Mitchell, M. Mulheron, J. Tritt-Goc, D. Verganelakis, Magnetic resonance studies of cement based materials in inhomogeneous magnetic fields. *Cem Conc Res.* 35 (2005) 2033–2040.
- [2] S. Kerkhofs, H. Lipkens, F. Velghe, P. Verlooy, J. Martens, Mayonnaise production in batch and continuous process exploiting magnetohydrodynamic force. *J Food Eng.* 106 (2011) 35-39.
- [3] M. Sheikholeslami, H. B. Rokni, Simulation of nanofluid heat transfer in presence of magnetic field: A review. *Int. J. Heat & Mass Transfer*, 115 (2017) 1203–1233
- [4] M. A. Waheed, Mixed convective heat transfer in rectangular enclosures driven by a continuously moving horizontal plate. *Int. J. Heat & Mass Transfer*, 52 (2009) 5055–5063.
- [5] R. Iwatsu, J. M. Hyun, K. Kuwahara, Mixed convection in a driven cavity with a stable vertical temperature gradient. *Int. J. Heat & Mass Transfer*, 36 (1993) 1601–1608.
- [6] M. A. R. Sharif, Laminar mixed convection in shallow inclined driven cavities with hot moving lid on top and cooled from bottom. *Appl. Thermal Engrg.* 27 (2007) 1036–1042.
- [7] K. Khanafer, A. M. Al-Amiri, I. Pop, Numerical simulation of unsteady mixed convection in a driven cavity, using an externally excited sliding lid. *Euro. J. Mech - B/Fluids*, 26 (2007) 669–687.
- [8] R. K. Tiwari, M. K. Das, Heat transfer augmentation in a two-sided lid-driven differentially heated square cavity utilizing nanofluids. *Int. J. Heat & Mass Transfer*, 50 (2007) 2002–2018.
- [9] M. M. Abdelkhalek, Mixed convection in a square cavity by a perturbation technique. *Comp. Mat. Sci.* 42 (2008) 212–219.
- [10] H. F. Oztop, Z. Zhao, B. Yu, Conduction-combined forced and natural convection in lid-driven enclosures divided by a vertical solid partition, *Int. Commun. Heat Mass Transfer*, 36 (2009) 661–668.
- [11] K. M. Khanafer, A.J. Chamkha, Mixed Convection Flow in a Lid-Driven Enclosure Filled with a Fluid-Saturated Porous Medium, *International Journal of Heat and Mass Transfer*, 42 (1999) 2465–2481.
- [12] T. Basak, S. Roy, A. J. Chamkha, Peclet Number based Analysis of Mixed Convection for Lid- Driven Porous Square Cavities with Various Heating of Bottom Wall, *International Communications in Heat and Mass Transfer*, 39 (2012) 657–664.
- [13] E. Abu-Nada, A. J. Chamkha, Mixed Convection Flow of a Nanofluid in a Lid-Driven Cavity with a Wavy Wall, *International Communications in Heat and Mass Transfer*, 57 (2014) 36–47.



- [14] A. Alsabery, M. Ismael, A. J. Chamkha, I. Hashim, Mixed Convection of Al<sub>2</sub>O<sub>3</sub>-Water Nanofluid in a Double Lid-Driven Square Cavity with a Solid Inner Insert using Buongiorno's Two-Phase Model, *International Journal of Heat and Mass Transfer*, 119 (2018) 939–961.
- [15] M. Hatami, J. Zhou, J. Geng, D. Song, D. Jing, Optimization of a lid-driven T-shaped porous cavity to improve the nanofluids mixed convection heat transfer, *Journal of Molecular Liquids* 231 (2017) 620–631.
- [16] M. Sathiyamoorthy, A. Chamkha, Effect of magnetic field on natural convection flow in a liquid gallium filled square cavity for linearly heated side wall(s), *Int. J. Therm. Sci.*, 49 (2010) 1856–1865.
- [17] S. Sivasankaran, A. Malleswaran, J. Lee, P. Sundar, Hydro-magnetic combined convection in a lid-driven cavity with sinusoidal boundary conditions on both sidewalls, *Int. J. Heat Mass Transfer*, 54 (2011) 512–525.
- [18] M. M. Rahman, S. Parvin, R. Saidur, N. A. Rahim, Magnetohydrodynamic mixed convection in a horizontal channel with an open cavity, *Int. Commun. Heat Mass Transfer*, 38 (2011) 184–193.
- [19] H. F. Oztop, K. Al-Salem, I. Pop, MHD mixed convection in a lid-driven cavity with corner heater, *Int. J. Heat Mass Transfer*, 54 (2011) 3494–3504.
- [20] R. Nasrin, S. Parvin, Hydromagnetic effect on mixed convection in a lid-driven cavity with sinusoidal corrugated bottom surface, *Int. Commun. Heat Mass Transfer*, 38 (2011) 781–789.
- [21] GH.R. Kefayati, M. Gorji-Bandpy, H. Sajjadi, D.D. Ganji, Lattice Boltzmann simulation of MHD mixed convection in a lid-driven square cavity with linearly heated wall, *Scientia Iranica B* (2012) 19 (4), 1053–1065.
- [22] H. Sajjadi, M. Gorji-Bandpy, D. D. Ganji, GH. R. Kefayati, Lattice Boltzmann simulation of MHD mixed convection in a two-sided lid-driven square cavity, *Heat Transfer–Asian Research* (2011) 41 (2), 179–195.
- [23] H. Sajjadi, GH.R. Kefayati, MHD Turbulent and Laminar Natural Convection in a Square Cavity utilizing Lattice Boltzmann Method, *Heat Transfer–Asian Research* 45 (2015) 795–814.
- [24] Hamid Reza Ashorynejad, Kurosh Sedighi, Mousa Farhadi, Ehsan Fattahi, Simulating magnetohydrodynamic natural convection flow in a horizontal cylindrical annulus using the lattice Boltzmann method, *Heat Transfer–Asian Research* 41 (2012) 468–483.
- [25] Hamid Reza Ashorynejad, Abdulmajeed A. Mohamad, Mohsen Sheikholeslami, Magnetic field effects on natural convection flow of a nanofluid in a horizontal cylindrical annulus using Lattice Boltzmann method, *International Journal of Thermal Sciences* 64 (2013) 240–250.
- [26] R. Yousofvand, S. Derakhshan, K. Ghasemi, M. Siavashi, MHD transverse mixed convection and entropy generation study of electromagnetic pump

- including a nanofluid using 3D LBM simulation, *International Journal of Mechanical Sciences* 133 (2017) 73–90.
- [27] S. A. M. Mehryan, Mohammad Ghalambaz, Muneer A. Ismael, Ali J. Chamkha, Analysis of fluid-solid interaction in MHD natural convection in a square cavity equally partitioned by a vertical flexible membrane, *Journal of Magnetism and Magnetic Materials* 424 (2017) 161–173.
- [28] Mohammad Ghalambaz, Ali Doostanidezfuli, Hossein Zargartalebi, Ali J. Chamkha, MHD phase change heat transfer in an inclined enclosure: Effect of a magnetic field and cavity inclination, *Numerical Heat Transfer, Part A: Applications* 71 (2017) 91–109.
- [29] Fatih Selimefendigil, Hakan F. Oztop, Numerical study of MHD mixed convection in a nanofluid filled lid driven square enclosure with a rotating cylinder, *International Journal of Heat and Mass Transfer* 78 (2014) 741–754.
- [30] Fatih Selimefendigil, Hakan F. Oztop, Conjugate natural convection in a nanofluid filled partitioned horizontal annulus formed by two isothermal cylinder surfaces under magnetic field, *International Journal of Heat and Mass Transfer* 108 (2017) 156–171.
- [31] Nadezhda S. Bondareva, Mikhail A. Sheremet, Natural convection heat transfer combined with melting process in a cubical cavity under the effects of uniform inclined magnetic field and local heat source, *International Journal of Heat and Mass Transfer* 108 (2017) 156–171.
- [32] Nikita S. Gibanov, Mikhail A. Sheremet, Hakan F. Oztop, Nidal Abu-Hamdeh, Effect of uniform inclined magnetic field on mixed convection in a lid-driven cavity having a horizontal porous layer saturated with a ferrofluid, *International Journal of Heat and Mass Transfer* 114 (2017) 1086–1097.
- [33] Jong Hyeon Son, Il Seouk Park, Numerical study of MHD natural convection in a rectangular enclosure with an insulated block, *Numerical Heat Transfer, Part A* 71 (2017) 1004–1022.
- [34] M. Hatami, J. Zhou, J. Geng, D. Jing, Variable magnetic field (VMF) effect on the heat transfer of a half-annulus cavity filled by Fe<sub>3</sub>O<sub>4</sub>-water nanofluid under constant heat flux, *Journal of Magnetism and Magnetic Materials* 451 (2018) 173–182.
- [35] A.J. Chamkha, Hydromagnetic Combined Convection Flow in a Vertical Lid-Driven Cavity Enclosure with Internal Heat Generation or Absorption, *Numerical Heat Transfer, Part A*, 41 (2002) 529–546.
- [36] M. Sheikholeslami, A.J. Chamkha, Flow and Convective Heat Transfer of a Ferro-Nanofluid in a Double-Sided Lid-Driven Cavity with a Wavy Wall in the Presence of a Variable Magnetic Field, *Numerical Heat Transfer, Part A*, 69 (2016) 1186–1200.
- [37] A.M. Rashad, M. Ismael, A.J. Chamkha and M.A. Mansour, MHD Mixed Convection of Localized Heat Sources in a Nanofluid-Filled Lid-Driven Square

- Cavity with Partial Slip, *Journal of the Taiwan Institute of Chemical Engineers*, 68 (2016) 173–186.
- [38] F. Selimefendigil, H. Oztop and A.J. Chamkha, FluidStructure-Magnetic Field Interaction in a Nanofluid Filled Lid-Driven Cavity with Flexible Side Wall, *European Journal of Mechanics B/Fluids*, 61 (2017) 77–85.
- [39] F. Selimefendigil and A.J. Chamkha, MHD Mixed Convection in a Lid-Driven Cavity Having a Corrugated Bottom Wall and Filled with a Non-Newtonian Power-Law Fluid Under the Influence of an Inclined Magnetic Field, *ASME Journal of Thermal Science and Engineering Applications*, 8 (2016) 021023-1—021023-8.
- [40] A. J. Chamkha, A. M. Rashad, M. A. Mansour, T. Armaghani, M. Ghalambaz, Effects of heat sink and source and entropy generation on MHD mixed convection of a Cu-water nanofluid in a lid-driven square porous enclosure with partial slip, *Physics of Fluids*, 29, 052001 (2017).
- [41] A. Yadollahi, A. Khalesidoost, A. Kasaeipoor, M. Hatami, D. Jing, Physical investigation on silver-water nanofluid natural convection for an F-shaped cavity under the magnetic field effects, *The European Physical Journal Plus* 132 (2017) 372.
- [42] M. Tahari, A. Ghorbanian, M. Hatami, D. Jing, Physical effect of a variable magnetic field on the heat transfer of a nanofluid-based concentrating parabolic solar collector, *The European Physical Journal Plus* 132 (2017) 549.
- [43] Gholamreza Kefayat, (2017) Simulation of the Flows of Incompressible Bingham Fluids using Macroscopic and Mesoscopic Methods: Isothermal and Non-Isothermal Problems, PhD Thesis, Flinders University.  
(<https://theses.flinders.edu.au/view/f9f8232b-0a4f-42a7-bc6c-4e329f0e58a4/1>).
- [44] F. J. Sanchez, Application of a first-order operator splitting method to Bingham fluid flow simulation. *Comp. Math. Appl.* 36 (1998) 71–86.
- [45] E. J. Dean, R. Glowinski, Operator-splitting methods for the simulation of Bingham visco-plastic flow. *Chinese Annal. Math.* 23B (2002) 187–204.
- [46] E. Mitsoulis, T. Zisis, Flow of Bingham plastics in a lid-driven square cavity. *J. Non-Newt. Fluid Mech.* 101 (2001) 173–180.
- [47] P. Neofytou, A 3rd order upwind finite volume method for generalised Newtonian fluid flows. *Adv. Engrg. Software, Part A* 36 (2005) 664–680.
- [48] D. Vola, L. Boscardin, J. Latch, Laminar unsteady flows of Bingham fluids: a numerical strategy and some benchmark results. *J Comput Phys* 2003; 187: 441–456.
- [49] R. R. Huilgol, Z. You, Prolegomena to variational inequalities and numerical schemes for compressible viscoplastic fluids. *J. Non-Newtonian Fluid Mech.* 2009; 158: 113–126.

- [50] D. Santos, S. Frey, M. Naccache, P. Souza Mendes, Numerical approximations for flow of viscoplastic fluids in a lid-driven cavity. *J Non-Newtonian Fluid Mech* 2011; 166: 667–679.
- [51] A. Syrakos, G. C. Georgiou, A. N. Alexandrou, Performance of the finite volume method in solving regularised Bingham flows: inertia effects in the lid-driven cavity flow. *J. Non-Newt. Fluid Mech.* 208-209 (2014) 88–107.
- [52] Osman Turan, Nilanjan Chakraborty, Robert J. Poole, Laminar natural convection of Bingham fluids in a square enclosure with differentially heated side walls, *J. Non-Newtonian Fluid Mech.* 165 (2010) 901-913.
- [53] Osman Turan, Robert J. Poole, Nilanjan Chakraborty, Aspect ratio effects in laminar natural convection of Bingham fluids in rectangular enclosures with differentially heated side walls. *J. Non-Newt. Fluid Mech.*, 166 (2011) 208-230.
- [54] Osman Turan, Nilanjan Chakraborty, Robert J. Poole, Laminar Rayleigh-Bnard convection of yield stress fluids in a square enclosure. *J. Non-Newt. Fluid Mech.*, 171-172 (2012) 83-96.
- [55] R.R. Huilgol, G.H.R. Kefayati, Natural convection problem in a Bingham fluid using the operator-splitting method, *Journal of Non-Newtonian Fluid Mechanics* 220 (2015) 22-32.
- [56] I. Karimfazli, I. A. Frigaard, A. Wachs, A novel heat transfer switch using the yield stress, *Journal of Fluid Mechanics* 783 (2015) 526-566.
- [57] A. K. Baranwal, R. P. Chhabra, Effect of fluid Yield stress on natural convection from horizontal cylinders in a square enclosure, *Heat Transfer Engineering* 38 (2017) 557-577
- [58] Ashin Dutta , Anoop K. Gupta , Garima Mishra , R.P. Chhabra, Effect of fluid yield stress and of angle of tilt on natural convection from a square bar in a square annulus, *Computers and Fluids* 160 (2018) 138-163.
- [59] GH. R. Kefayati, Double-diffusive natural convection and entropy generation of Bingham fluid in an inclined cavity, *International Journal of Heat and Mass Transfer* 116 (2018) 762–812.
- [60] GH. R. Kefayati, H. Tang, Mesoscopic simulation of double-diffusive natural convection and entropy generation of Bingham fluid in an open cavity, *European Journal of Mechanics / B Fluids* 69 (2018) 1–45.
- [61] GH. R. Kefayati, H. Tang, Lattice Boltzmann simulation of viscoplastic fluids on natural convection in an inclined enclosure with inner cold circular/elliptical cylinders (Part I: One cylinder), *International Journal of Heat and Mass Transfer* (In Press)(<https://doi.org/10.1016/j.ijheatmasstransfer.2018.01.139>).
- [62] GH. R. Kefayati, H. Tang, Lattice Boltzmann simulation of viscoplastic fluids on natural convection in an inclined enclosure with inner cold circular/elliptical cylinders (Part II: Two cylinders), *International Journal of Heat and Mass Transfer* (In Press) (<https://doi.org/10.1016/j.ijheatmasstransfer.2018.01.137>).

- [63] GH. R. Kefayati, H. Tang, Lattice Boltzmann simulation of viscoplastic fluids on natural convection in an inclined enclosure with inner cold circular/elliptical cylinders (Part III: Four cylinders), *International Journal of Heat and Mass Transfer* (In Press) (<https://doi.org/10.1016/j.ijheatmasstransfer.2018.01.140>).
- [64] S. Mukherjee, A. K. Gupta, R. P. Chhabra, Laminar forced convection in power-law and Bingham plastic fluids in ducts of semi-circular and other cross-sections, *International Journal of Heat and Mass Transfer* 104 (2017) 112–141.
- [65] A. K. Gupta, R. P. Chhabra, Mixed convection from a spheroid in Bingham plastic fluids: Effect of buoyancy-assisted flow, *Numerical Heat Transfer, Part A: Applications* 69 (2016) 898–920.
- [66] A. H. Raja, S. A. Patel, R. P. Chhabra, Laminar forced convection heat transfer from a two-dimensional transverse plate in Bingham plastic fluids, *International Journal of Heat and Mass Transfer* 83 (2015) 690–709.
- [67] GH. R. Kefayati, R. R. Huilgol, Lattice Boltzmann Method for simulation of mixed convection of a Bingham fluid in a lid-driven cavity, *International Journal of Heat and Mass Transfer* 103 (2016) 725–743.
- [68] S. Chen, Gary D. Doolen, Lattice Boltzmann Method for fluid flows, *Annu. Rev. Fluid Mech.* 30 (1998) 329–364.
- [69] Cyrus K. Aidun, Jonathan R. Clausen, Lattice-Boltzmann Method for Complex Flows, *Annu. Rev. Fluid Mech.* 42 (2010) 439–472.
- [70] Zhaoli Guo, T. S. Zhao, Lattice Boltzmann model for incompressible flows through porous media, *Physical Review E* 66, 036304 (2002).
- [71] A. A. Mohamad, (2011); *Lattice Boltzmann method: fundamentals and engineering applications with computer codes*, Springer Science & Business Media.
- [72] A. A. Mehrizi, M. Farhadi, S. Shayamehr, Natural convection flow of Cu-Water nanofluid in horizontal cylindrical annuli with inner triangular cylinder using lattice Boltzmann method, *International Communications in Heat and Mass Transfer* 44 (2013) 147–156.
- [73] Hamid Reza Ashorynejad, Ahad Zarghami, Magnetohydrodynamics flow and heat transfer of Cu-water nanofluid through a partially porous wavy channel, *International Journal of Heat and Mass Transfer* 119 (2018) 247–258.
- [74] H. Sajjadi, M. Salmanzadeh, G. Ahmadi, S. Jafari, Turbulent indoor airflow simulation using hybrid LES/RANS model utilizing Lattice Boltzmann method, *Computers and Fluids* 150 (2017) 66–73.
- [75] Hamid Reza Ashorynejad, B. Hoseinpour, Investigation of different nanofluids effect on entropy generation on natural convection in a porous cavity, *European Journal of Mechanics-B/Fluids* 62 (2018) 86–93.

- [76] Hamid Reza Ashorynejad, Koroush Javaherdeh, Investigation of a waveform cathode channel on the performance of a PEM fuel cell by means of a pore-scale multi-component lattice Boltzmann method, *Journal of the Taiwan Institute of Chemical Engineers* 66 (2016) 126–136.
- [77] S.C. Fu, R.M.C. So, W.W.F. Leung, Linearized-Boltzmann-type-equation based finite difference method for thermal incompressible flow, *Computers and Fluids* 69 (2012) 67–80.
- [78] R.R. Huilgol, GH.R. Kefayati, From mesoscopic models to continuum mechanics: Newtonian and non-Newtonian fluids, *Journal of Non-Newtonian Fluid Mechanics* 233 (2016) 146–154.
- [79] R. R. Huilgol, GH. R. Kefayati, A particle distribution function approach to the equations of continuum mechanics in Cartesian, cylindrical and spherical coordinates: Newtonian and non-Newtonian Fluids, *Journal of Non-Newtonian Fluid Mechanics* 251 (2018) 119–131.
- [80] GH. R. Kefayati, R.R. Huilgol, Lattice Boltzmann method for the simulation of the steady flow of a Bingham fluid in a pipe of square cross-section, *European Journal of Mechanics B Fluids* 65 (2017) 412-422.
- [81] B. Knaepen, S. Kassinos, D. Carati, Magnetohydrodynamic turbulence at moderate magnetic Reynolds number, *J. Fluid Mech.* 513 (2004) 199–220.
- [82] Mahendra K Verma, Anisotropy in Quasi-Static Magnetohydrodynamic Turbulence, *Rep. Prog. Phys.* 80 (2017) 087001 (31pp).
- [83] E. C. Bingham, *Fluidity and plasticity*, McGraw-Hill, New York (1922).
- [84] T. C. Papanastasiou, Flow of materials with yield, *J. Rheol.* 31 (1987) 385–404.
- [85] M. Bercovier, M. Engelman, A finite-element method for incompressible non-Newtonian flows, *J. Comput. Phys.*, 36 (1980) 313-326.
- [86] E. J. ODonovan, R.I. Tanner, Numerical study of the Bingham squeeze film problem, *J. Non-Newt. Fluid Mech.* 15 (1984) 75–83.
- [87] G. Duvaut, J. L. Lions, Transfert de chaleur dans un fluide de Bingham dont la viscosité dépend de la température. *J. Functional Anal.* 11 (1972) 93–110.
- [88] R. Glowinski, Finite element methods for incompressible viscous flow, in: *Handbook of Numerical Analysis*, 9 (2003) 3–1176.
- [89] R. R. Huilgol, *Fluid Mechanics of Viscoplasticity*. Springer, Berlin Heidelberg, 2015.
- [90] E. F. Toro, *Riemann Solvers and Numerical Methods for Fluid Dynamics: A Practical Introduction*. Springer, 1999, pp. 531–542.
- [91] P. D. Lax, B. Wendroff, Systems of conservation laws, *Comm. Pure Appl. Math.* 13 (1960) 217–237.

- [92] GH. R. Kefayati, FDLBM simulation of mixed convection in a lid-driven cavity filled with non-Newtonian nanofluid in the presence of magnetic field, *International Journal of Thermal Sciences* 95 (2015) 29–46.
- [93] GH. R. Kefayati, FDLBM simulation of magnetic field effect on mixed convection in a two sided lid-driven cavity filled with non-Newtonian nanofluid, *Powder Technology* 280 (2015) 576–588.
- [94] GH. R. Kefayati, Mesoscopic simulation of magnetic field effect on double-diffusive mixed convection of shear-thinning fluids in a two sided lid-driven cavity, *Journal of Molecular Liquids* 198 (2014) 413–429.
- [95] GH. R. Kefayati, Magnetic field effect on heat and mass transfer of mixed convection of shear-thinning fluids in a lid-driven enclosure with non-uniform boundary conditions, *Journal of the Taiwan Institute of Chemical Engineers* 51 (2015) 20–33.
- [96] Q. Zou, X. He, On pressure and velocity boundary conditions for the lattice Boltzmann BGK model. *Phys. Fluids*, 9 (1997) 1591–1598.
- [97] Z. Guo, B. Shi, C. Zheng, A coupled lattice BGK model for the Boussinesq equations. *Int. J. Numer. Methods Fluids*, 39 (2002) 325–342.
- [98] J. Blazek, *Computational Fluid Dynamics: Principles and Applications*. Elsevier, 2001, pp. 347–350.
- [99] T. Cebeci, J. P. Shao, F. Kafyeke, E. Laurendeau, *Computational Fluid Dynamics for Engineers*. Springer, 2005, pp. 311–320.

# Nomenclature

<b>A</b>	The first Rivlin-Ericksen tensor
AR	Aspect ratio of the cavity ( $AR = \frac{H}{L}$ )
Bn	Bingham number
$c$	Lattice speed
$c_p$	Specific heat capacity at constant pressure
<b>E</b>	Electric field strength
Ec	Eckert number
$F$	External forces
$f_\alpha$	Density distribution functions for the specific node of $\alpha$
$f_\alpha^{eq}$	Equilibrium density distribution functions for the specific node of $\alpha$
$g_\alpha$	Internal energy distribution functions for the specific node of $\alpha$
$g_\alpha^{eq}$	Equilibrium internal energy distribution functions for the specific node of $\alpha$
$g$	Gravity
Ha	Hartmann number
$H$	Enclosure height
<b>J</b>	Electric current density
$k$	Thermal conductivity
$L$	Enclosure width
<b>N</b>	Body force
Nu	Nusselt number
$p$	Pressure
Pr	Prandtl number
Re	Reynolds number
$T$	Temperature
$t$	Time
$x, y$	Cartesian coordinates
$u$	Velocity in x direction
$U_0$	The speed of the upper wall
$v$	Velocity in y direction

## Greek letters

$\beta_T$	Thermal expansion coefficient
$\phi$	Relaxation time
$\Phi$	Electrical potential
$\boldsymbol{\tau}$	Stress tensor
$\tau_y$	Yield stress
$\xi$	Discrete particle speeds
$\Delta x$	Lattice spacing in $x$ direction
$\Delta y$	Lattice spacing in $y$ direction



$\Delta t$	Time increment
$\alpha$	Thermal diffusivity
$\rho$	Density of fluid
$\sigma$	Electrical conductivity of the fluid
$\Lambda$	The viscoplasticity constraint
$\theta$	The inclined angle of the magnetic field

### Subscripts

<i>avg</i>	Average
<i>C</i>	Cold
<i>d</i>	Dynamic
<i>H</i>	Hot
<i>x, y</i>	Cartesian coordinates
$\alpha$	Specific node
<i>s</i>	Static

Table 1

Grid independence study at  $Re = 100$ ,  $Ha = 2$ ,  $Bn = 1$ ,  $Ec = 10^{-3}$ ,  $AR = 1$ , and  $\theta = 0^\circ$

Mesh size	$Nu_{avg}$	$ \psi_{max} $
120*120	2.7151	0.0676
140*140	2.5651	0.0688
160*160	2.5384	0.0690
180*180	2.5213	0.0694
200*200	2.5025	0.0696
220*220	2.5025	0.0696
240*240	2.5025	0.0696

Table 2

Comparison of the average Nusselt number on the hot wall for different aspect ratios and Hartmann numbers at  $Bn = 1$ ,  $\theta = 0^\circ$ ,  $Ec = 10^{-3}$ , and  $Re = 100$

	AR = 0.25	AR = 1	AR = 4
Ha = 0	12.8620	3.1302	2.1357
Ha = 2	11.7349	2.5025	1.4673
Ha = 5	9.5171	1.8705	1.2516

Table 3

Comparison of the average Nusselt number on the hot wall for different aspect ratios and Bingham numbers at  $Ha = 0$ ,  $Ec = 10^{-3}$ , and  $Re = 100$

	AR = 0.25	AR = 1	AR = 4
Bn = 1	12.8620	3.1302	2.1357
Bn = 5	11.0584	2.5025	1.3829
Bn = 10	9.8483	2.2201	1.3036

Table 4

Comparison of the average Nusselt number on the hot wall for different aspect ratios and Reynolds numbers at  $Ha = 2$ ,  $\theta = 0^\circ$ ,  $Ec = 10^{-3}$ , and  $Bn = 1$

	Re = 100	Re = 500	Re = 1000
AR = 0.25	11.7349	21.9304	26.6426
AR = 1	2.5025	4.9014	7.2560
AR = 4	1.4673	2.6241	3.7788

Table 5

Comparison of the average Nusselt number on the hot wall for different aspect ratios and magnetic field angles at  $\text{Ha} = 5$ ,  $\text{Re} = 100$ ,  $\text{Ec} = 10^{-3}$ , and  $\text{Bn} = 1$

	AR = 0.25	AR = 1	AR = 4
$\theta = 0^\circ$	9.5171	1.8705	1.2516
$\theta = 30^\circ$	9.0332	1.9716	1.2665
$\theta = 60^\circ$	7.0443	2.0727	1.3251
$\theta = 90^\circ$	6.4587	2.0483	1.7843

Table 6

Comparison of the average Nusselt number on the hot wall for different Eckert numbers and aspect ratios at  $Re = 100$ ,  $Bn = 1$ ,  $\theta = 0^\circ$ , and  $Ha = 5$

	$Ec = 0$	$Ec = 10^{-4}$	$Ec = 10^{-3}$	$Ec = 10^{-2}$
AR = 0.25	9.0488	9.0470	9.0332	8.8930
AR = 1	1.9730	1.9727	1.9716	1.9612
AR = 4	1.2672	1.2671	1.2665	1.2603

## List of Figures

Fig.1 Geometry of present study

Fig.2 The comparison of the isotherms, streamlines and yielded/unyielded parts in different non-dimensional time ( $t^*$ ) at  $Re = 1000$ ,  $Bn = 1$ ,  $AR = 0.25$ ,  $\theta = 0^\circ$ ,  $Ec = 10^{-3}$ , and  $Ha = 2$

Fig.3 Comparison of the isotherms for different aspect ratios and Hartmann numbers at  $Bn = 1$ ,  $\theta = 0^\circ$ ,  $Ec = 10^{-3}$ , and  $Re = 100$

Fig.4 Comparison of the streamlines for different aspect ratios and Hartmann numbers at  $Bn = 1$ ,  $\theta = 0^\circ$ ,  $Ec = 10^{-3}$ , and  $Re = 100$

Fig.5 Comparison of the yielded/unyielded sections for different aspect ratios and Hartmann numbers at  $Bn = 1$ ,  $\theta = 0^\circ$ ,  $Ec = 10^{-3}$ , and  $Re = 100$

Fig.6 Vertical velocity ( $v$ ) and temperature distribution ( $T$ ) at  $y = 0.5$ , horizontal velocity profile ( $u$ ) at  $x = 0.5$  and the local Nusselt number at the hot wall for different Hartmann numbers at  $Bn = 1$ ,  $\theta = 0^\circ$ ,  $AR = 1$ ,  $Ec = 10^{-3}$ , and  $Re = 100$

Fig.7 Comparison of the isotherms for different aspect ratios and Bingham numbers at  $Ha = 0$ ,  $Ec = 10^{-3}$ , and  $Re = 100$

Fig.8 Comparison of the streamlines for different aspect ratios and Bingham numbers at  $Ha = 0$ ,  $Ec = 10^{-3}$ , and  $Re = 100$

Fig.9 Comparison of the yielded/unyielded sections for different aspect ratios and Bingham numbers at  $Ha = 0$ ,  $Ec = 10^{-3}$ , and  $Re = 100$

Fig.10 Vertical velocity ( $v$ ) and temperature distribution ( $T$ ) at  $y = 0.5$ , horizontal velocity profile ( $u$ ) at  $x = 0.5$  and the local Nusselt number at the hot wall for different Bingham numbers at  $Ha = 0$ ,  $AR = 1$ ,  $Ec = 10^{-3}$ , and  $Re = 100$



Fig.11 Comparison of the isotherms, streamlines, and yielded/unyielded parts for different Reynolds numbers at  $Bn = 1$ ,  $Ha = 2$ ,  $AR = 1$ ,  $Ec = 10^{-3}$ , and  $\theta = 0^\circ$

Fig.12 Comparison of isotherms for different aspect ratios and magnetic field angles at  $Bn = 1$ ,  $Ha = 5$ ,  $Ec = 10^{-3}$ , and  $Re = 100$

Fig.13 Comparison of streamlines for different aspect ratios and magnetic field angles at  $Bn = 1$ ,  $Ha = 5$ ,  $Ec = 10^{-3}$ , and  $Re = 100$

Fig.14 Comparison of the yielded/unyielded parts for different aspect ratios and magnetic field angles at  $Bn = 1$ ,  $Ha = 5$ ,  $Ec = 10^{-3}$ , and  $Re = 100$

Fig.15 Comparison of the isotherms, streamlines, yielded/unyielded sections for different aspect ratios and Eckert numbers at  $Bn = 1$ ,  $Ha = 5$ ,  $\theta = 30^\circ$ , and  $Re = 100$  (The solid red line ( $Ec = 0.01$ ), and the dashed green line ( $Ec=10^{-4}$ ))

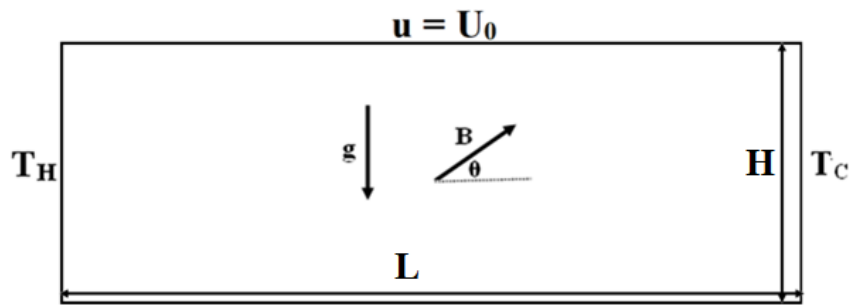


Fig. 1. Geometry of present study

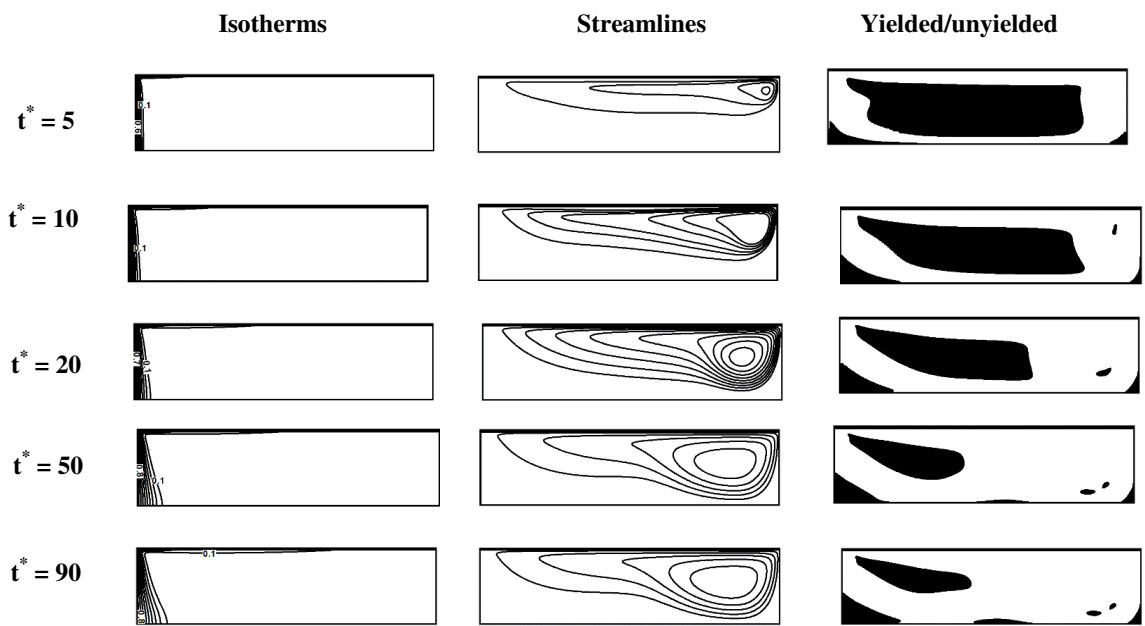


Fig. 2. The comparison of the isotherms, streamlines and yielded/unyielded parts in different non-dimensional time ( $t^*$ ) at  $Re = 1000$ ,  $Bn = 1$ ,  $AR = 0.25$ ,  $\theta = 0^\circ$ ,  $Ec = 10^{-3}$ , and  $Ha = 2$

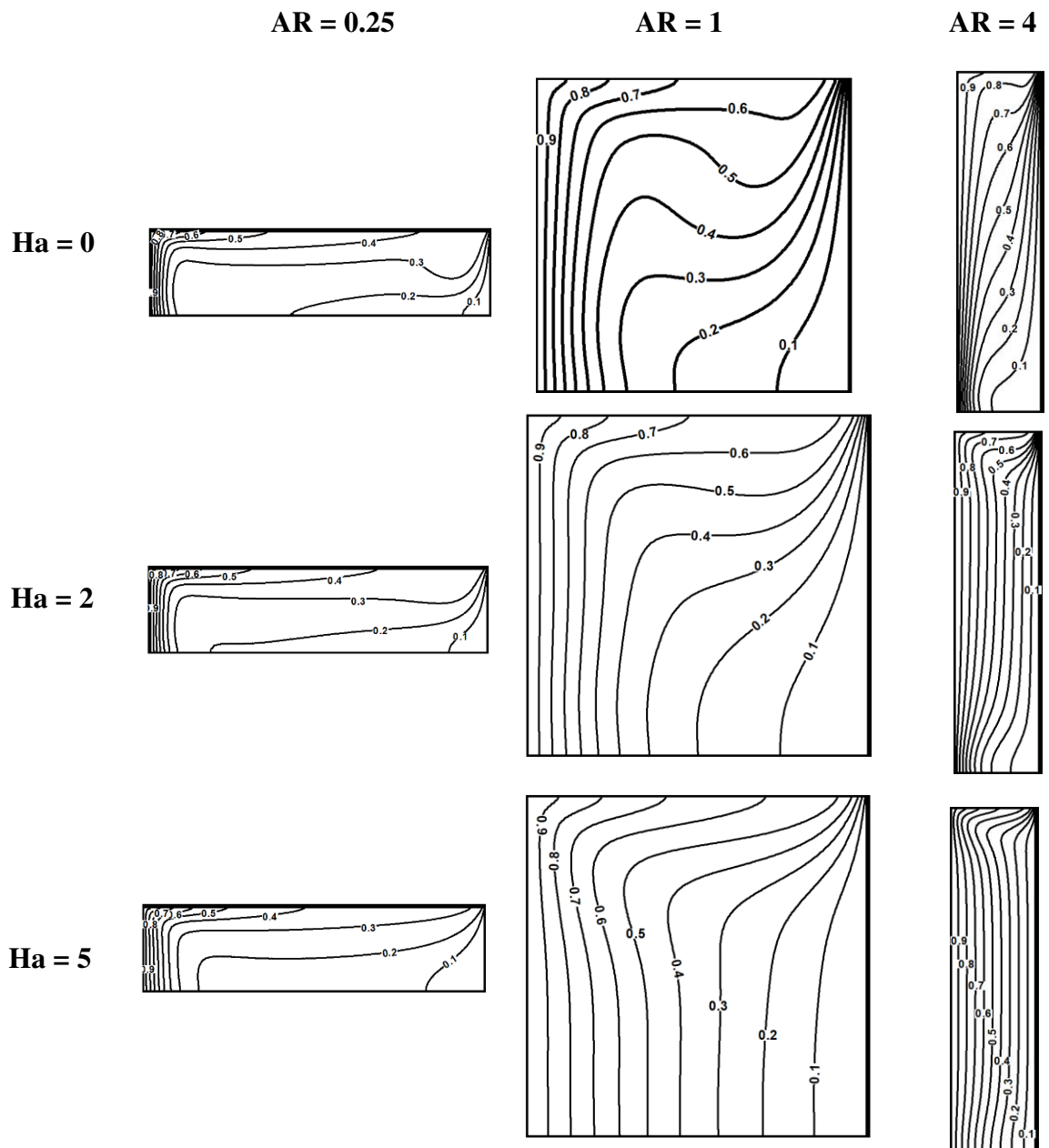


Fig. 3. Comparison of the isotherms for different aspect ratios and Hartmann numbers at  $Bn = 1$ ,  $\theta = 0^\circ$ ,  $Ec = 10^{-3}$ , and  $Re = 100$

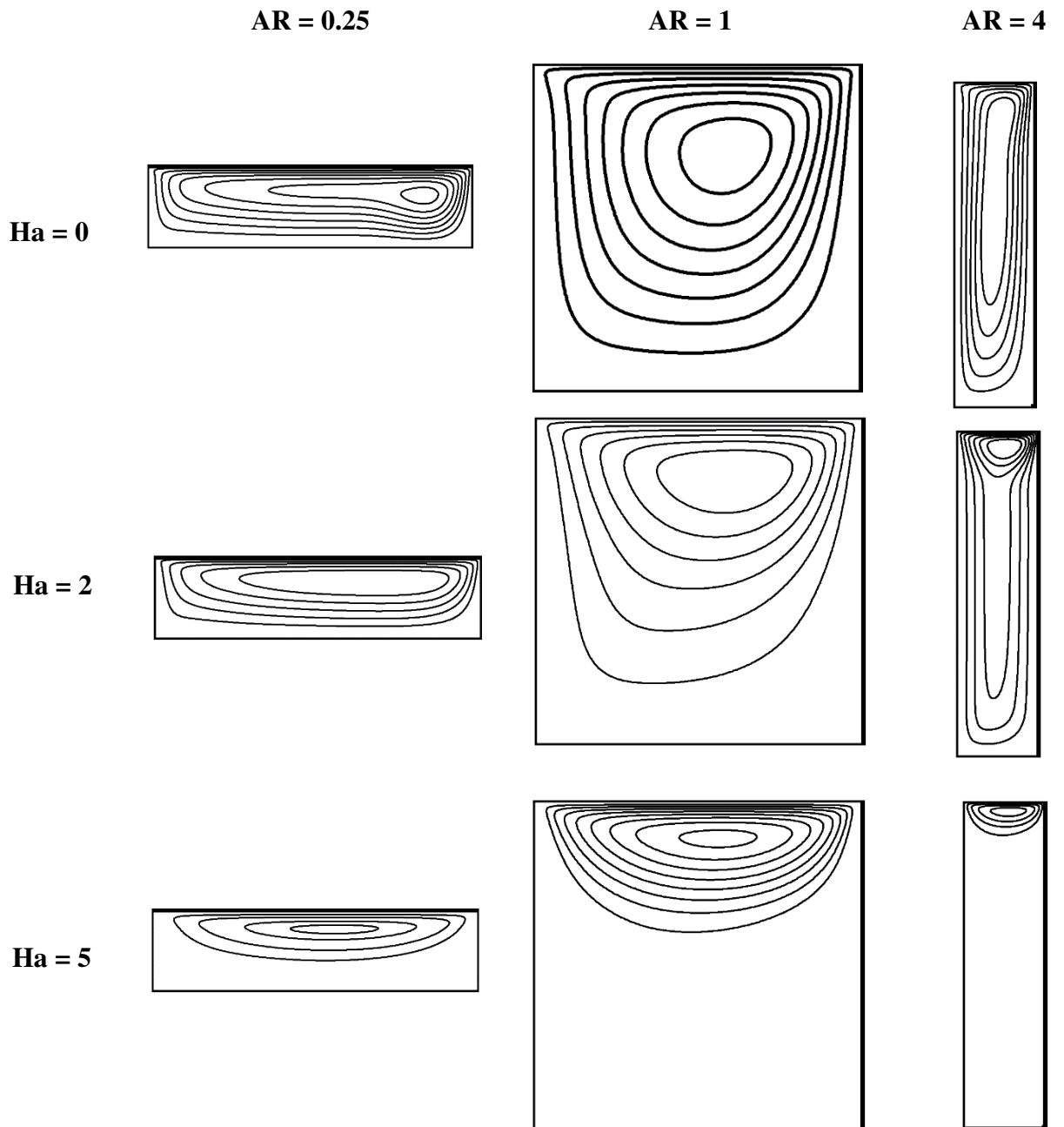


Fig. 4. Comparison of the streamlines for different aspect ratios and Hartmann numbers at  $Bn = 1$ ,  $\theta = 0^\circ$ ,  $Ec = 10^{-3}$ , and  $Re = 100$

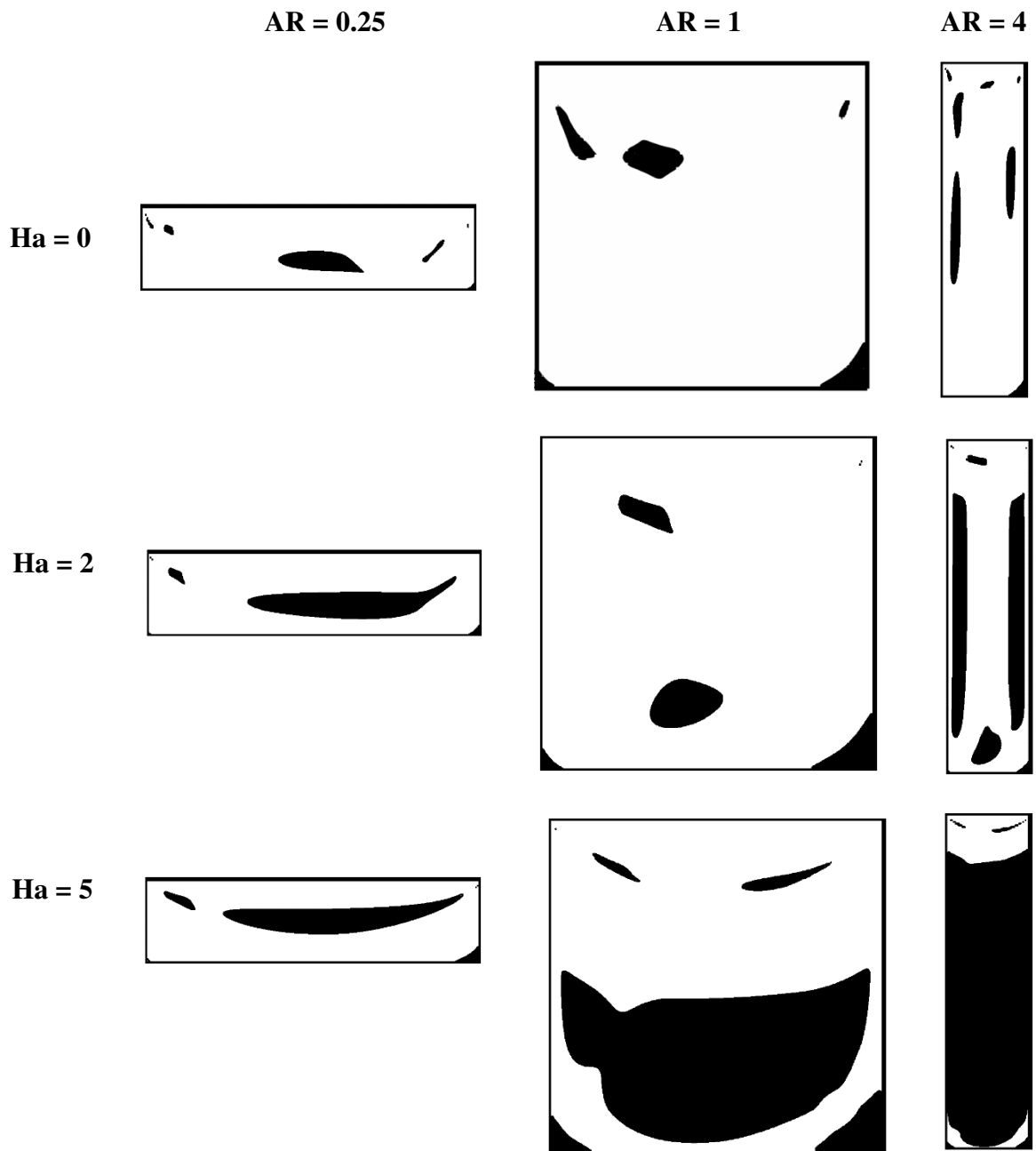


Fig. 5. Comparison of the yielded/unyielded sections for different aspect ratios and Hartmann numbers at  $Bn = 1$ ,  $\theta = 0^\circ$ ,  $Ec = 10^{-3}$ , and  $Re = 100$

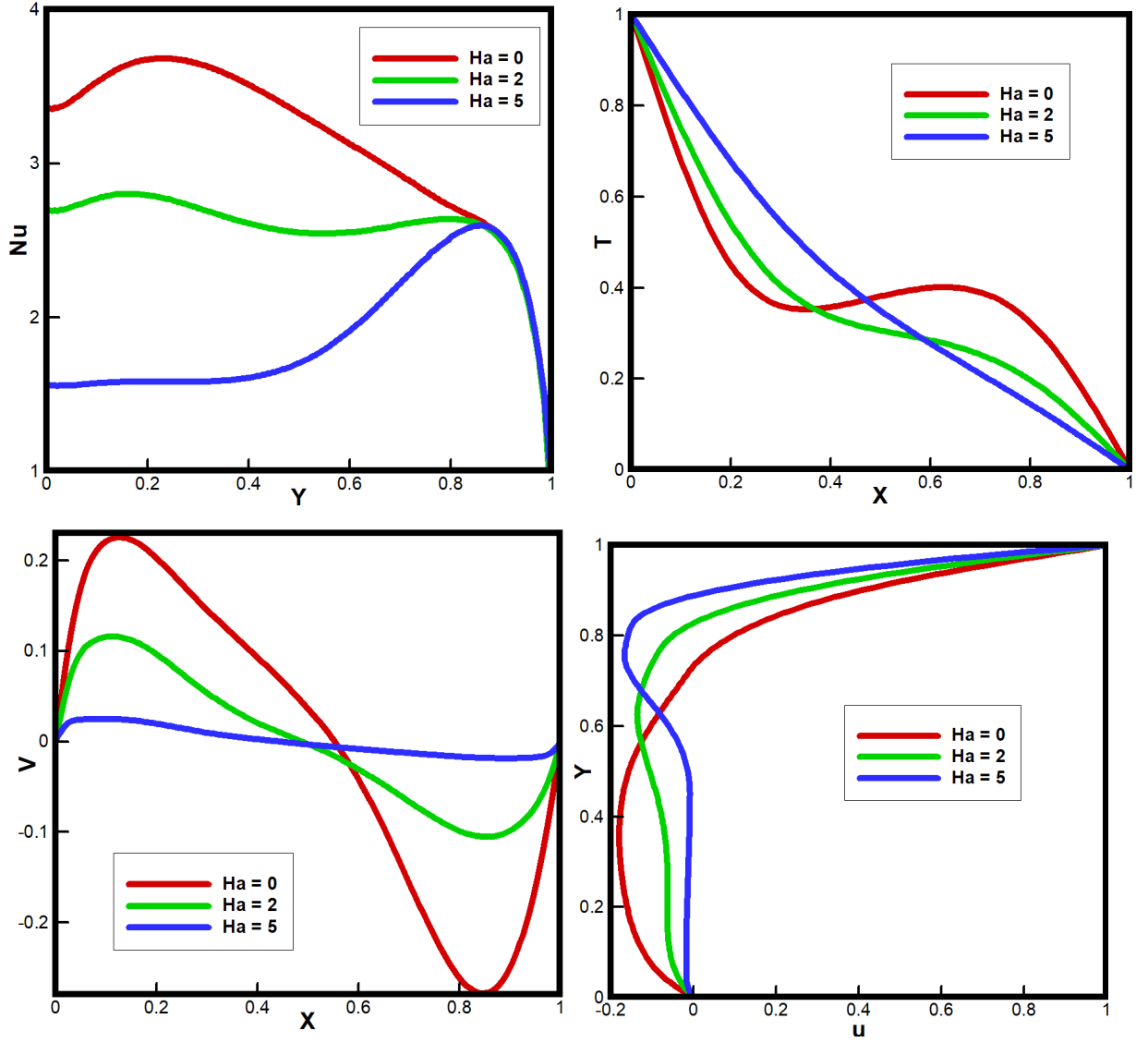


Fig. 6. Vertical velocity ( $v$ ) and temperature distribution ( $T$ ) at  $y = 0.5$ , horizontal velocity profile ( $u$ ) at  $x = 0.5$  and the local Nusselt number at the hot wall for different Hartmann numbers at  $Bn = 1$ ,  $\theta = 0^\circ$ ,  $AR = 1$ ,  $Ec = 10^{-3}$ , and  $Re = 100$

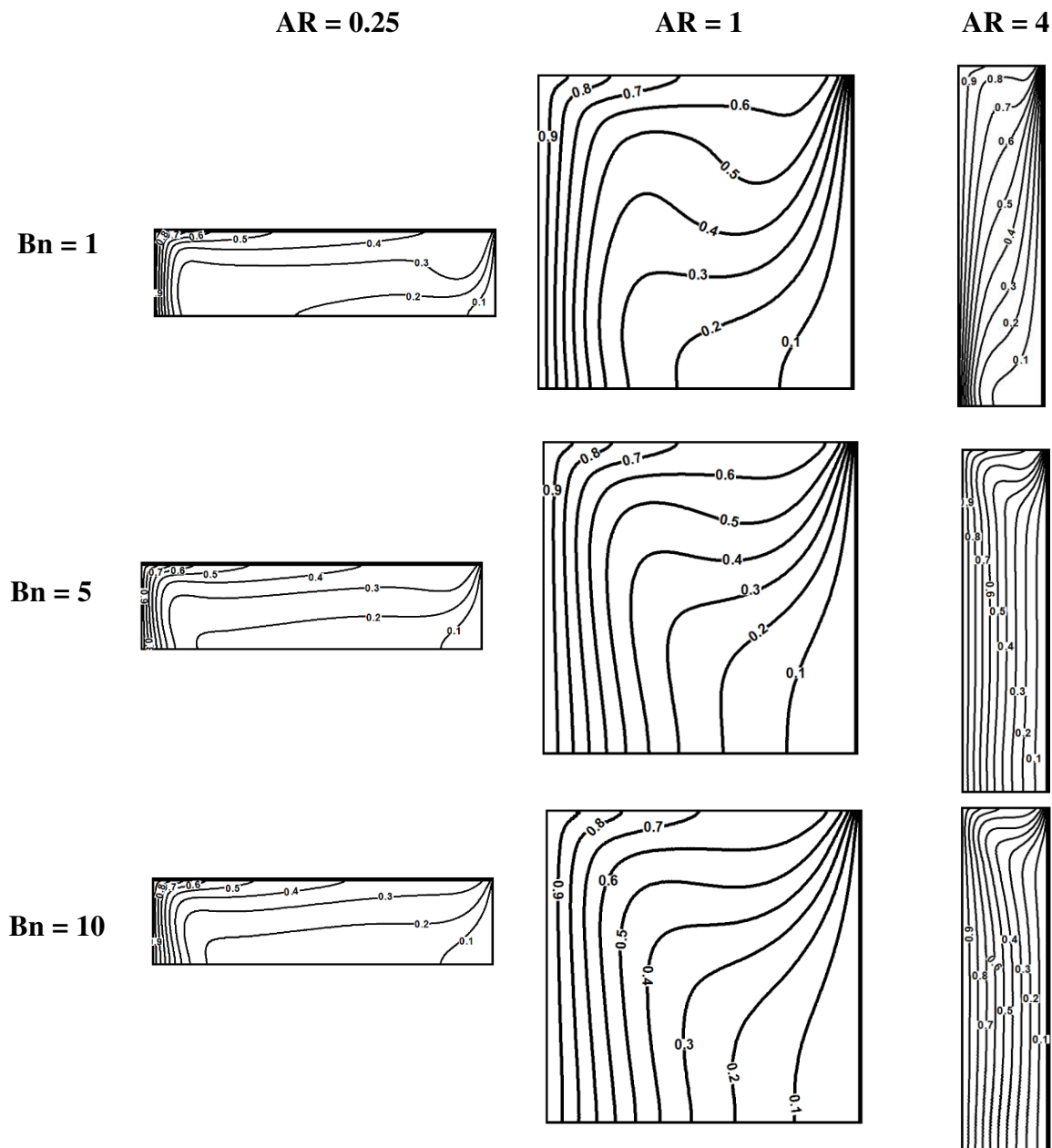


Fig. 7. Comparison of the isotherms for different aspect ratios and Bingham numbers at  $Ha = 0$ ,  $Ec = 10^{-3}$ , and  $Re = 100$



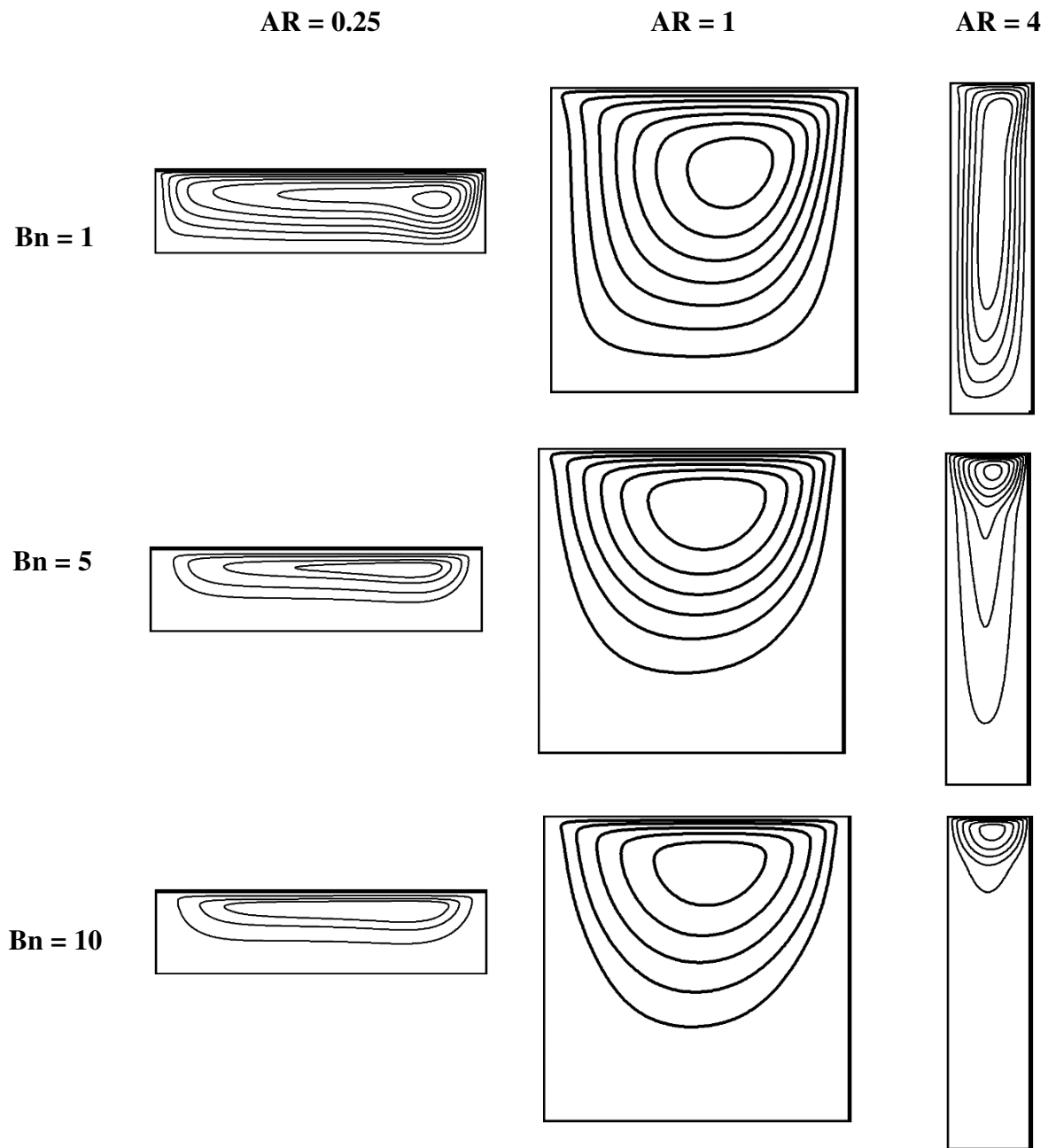


Fig. 8. Comparison of the streamlines for different aspect ratios and Bingham numbers at  $Ha = 0$ ,  $Ec = 10^{-3}$ , and  $Re = 100$

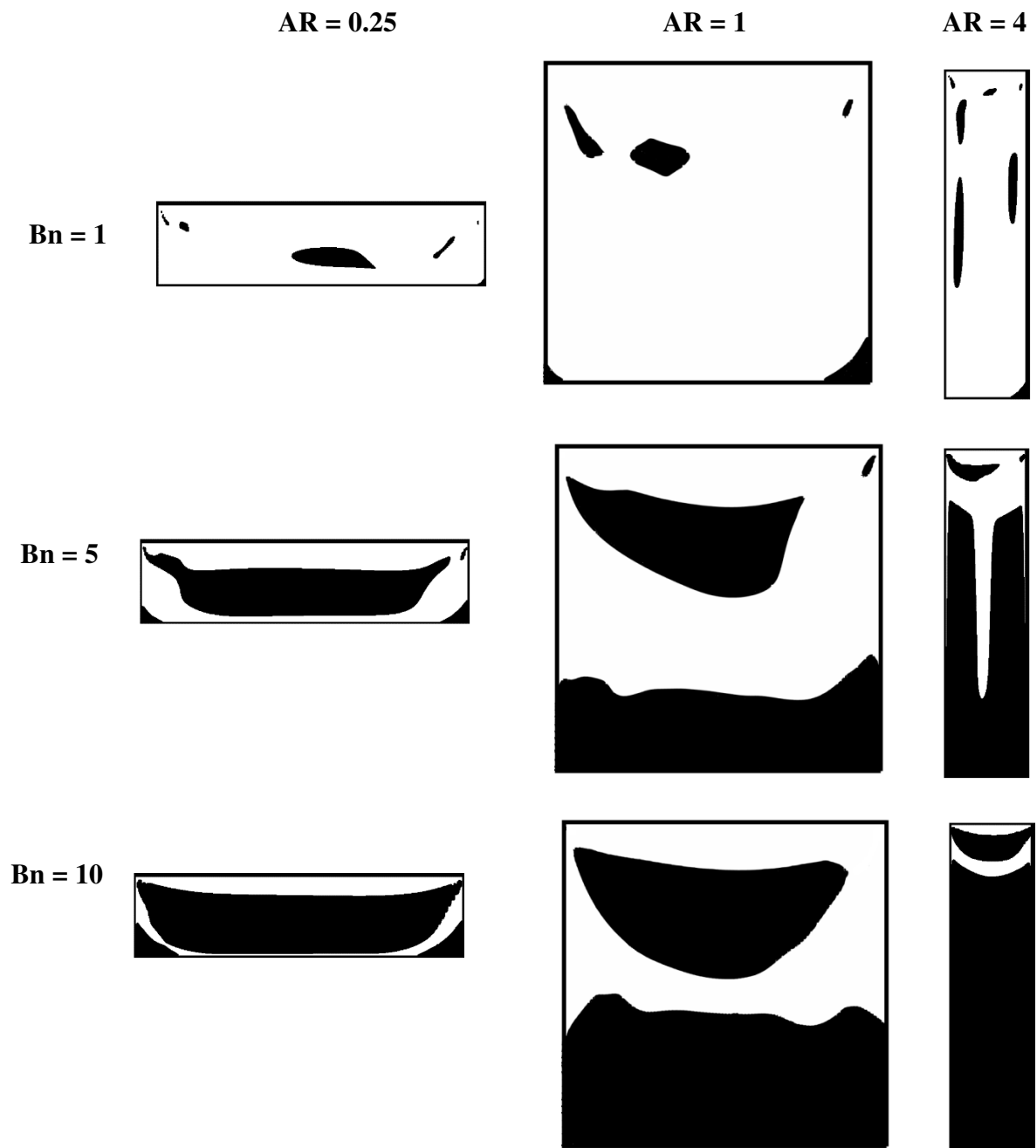


Fig. 9. Comparison of the yielded/unyielded parts for different aspect ratios and Bingham numbers at  $Ha = 0$ ,  $Ec = 10^{-3}$ , and  $Re = 100$

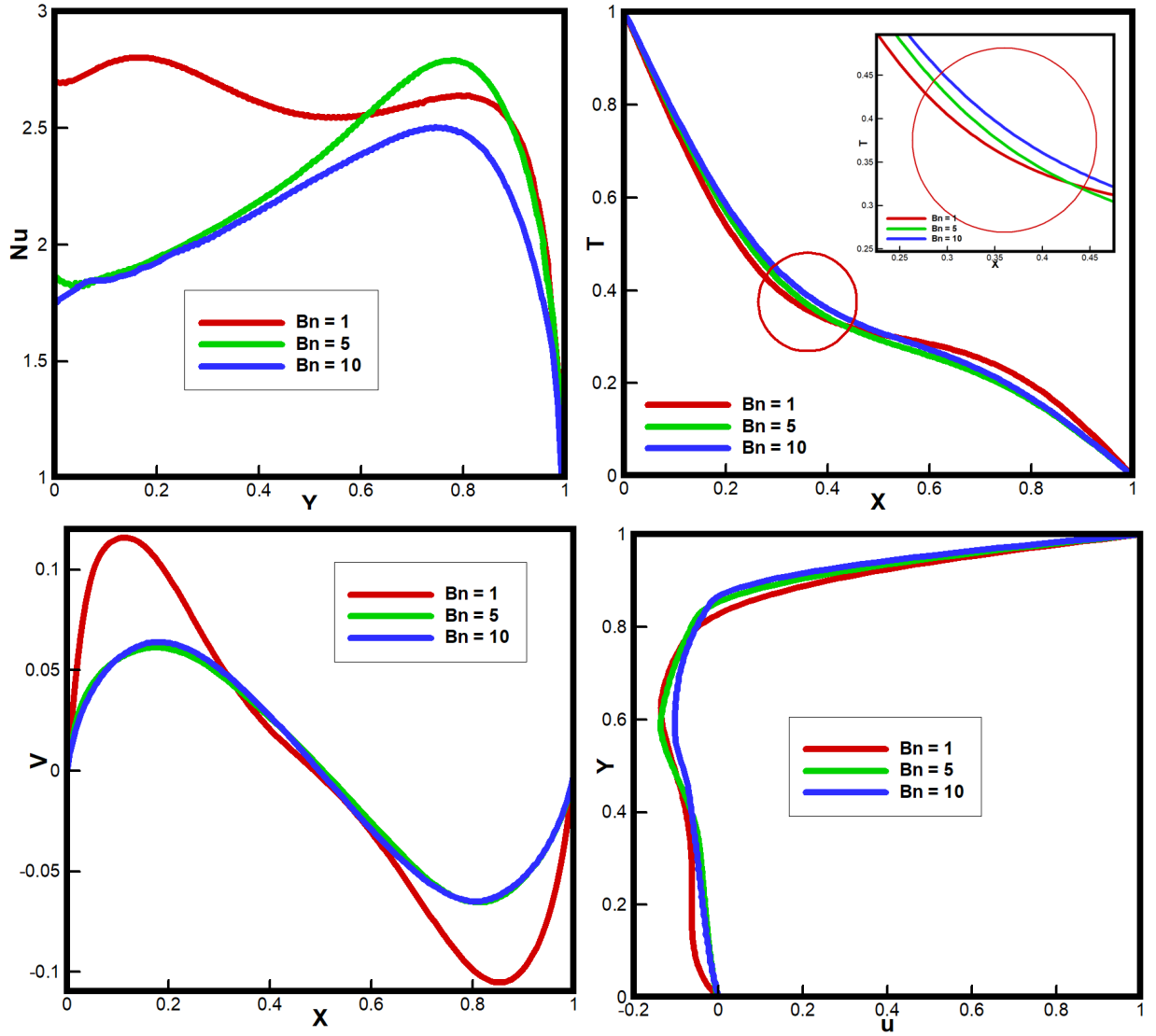


Fig. 10. Vertical velocity ( $v$ ) and temperature distribution ( $T$ ) at  $y = 0.5$ , horizontal velocity profile ( $u$ ) at  $x = 0.5$  and the local Nusselt number at the hot wall for different Bingham numbers at  $AR = 1$ ,  $Ha = 0$ ,  $Ec = 10^{-3}$ , and  $Re = 100$

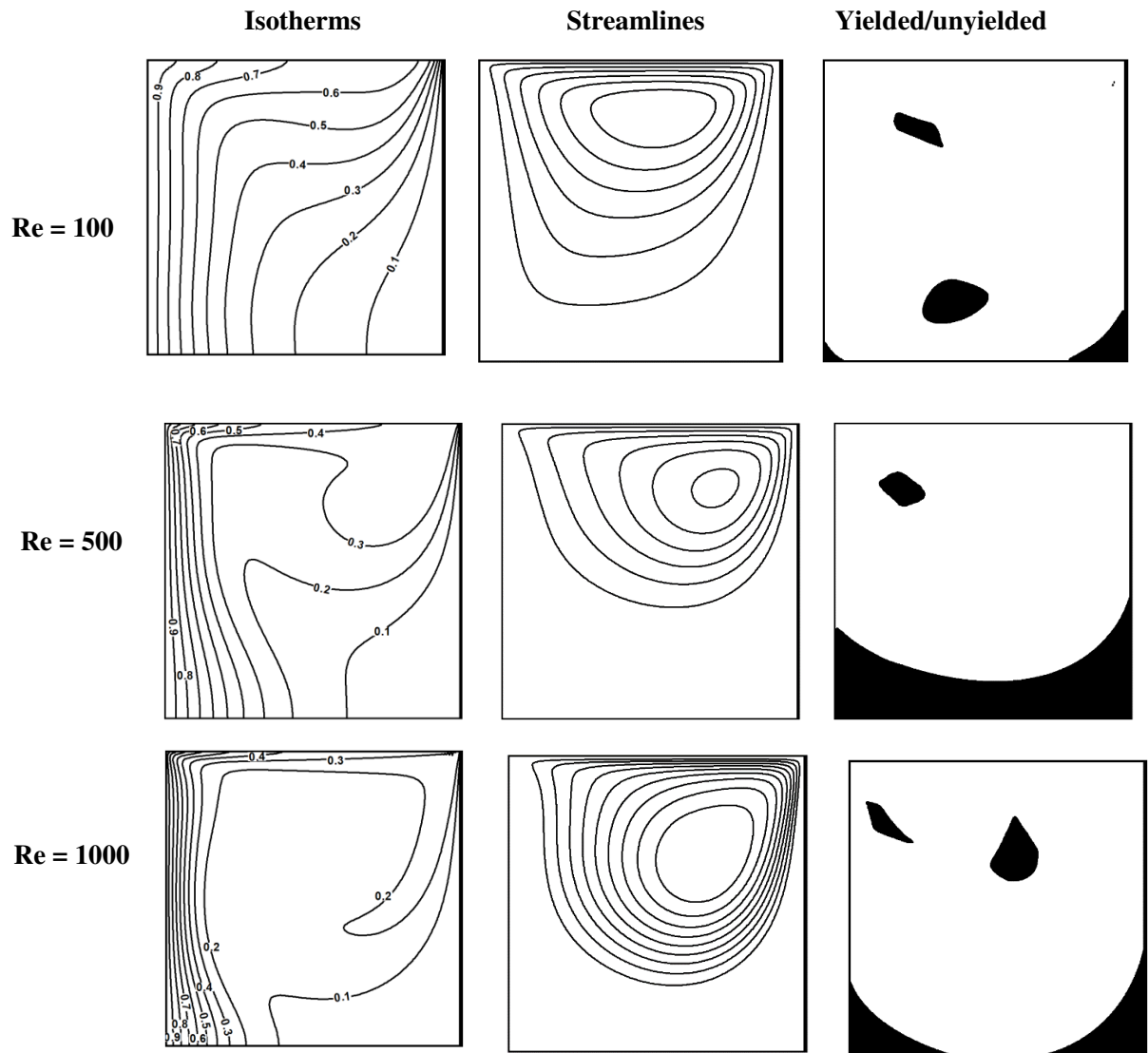


Fig. 11. Comparison of the isotherms, streamlines, and yielded/unyielded parts for different Reynolds numbers at  $Bn = 1$ ,  $Ha = 2$ ,  $AR = 1$ ,  $Ec = 10^{-3}$ , and  $\theta = 0^\circ$

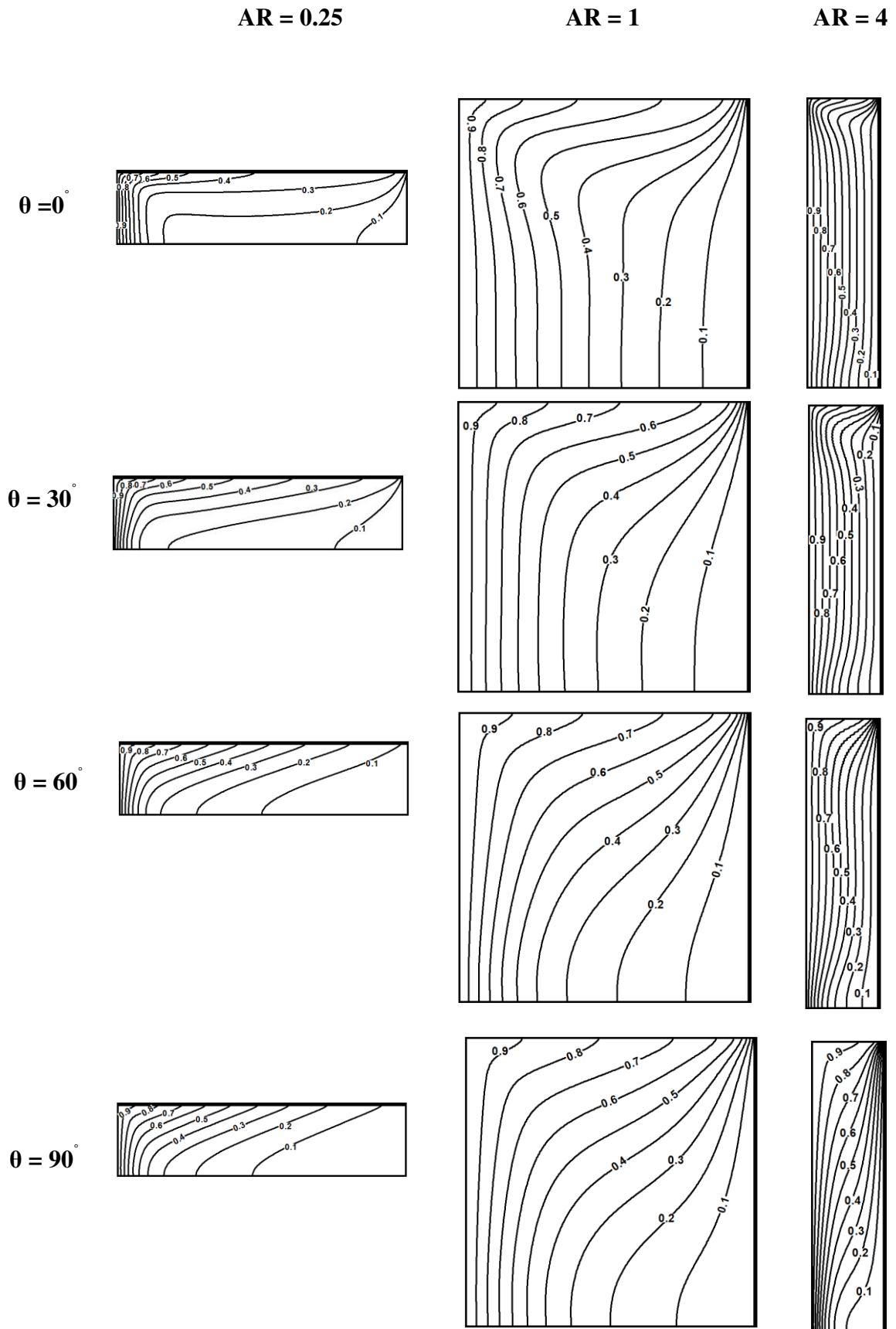


Fig. 12. Comparison of the isotherms for different aspect ratios and magnetic field angles at  $Bn = 1$ ,  $Ha = 5$ ,  $Ec = 10^{-3}$ , and  $Re = 100$

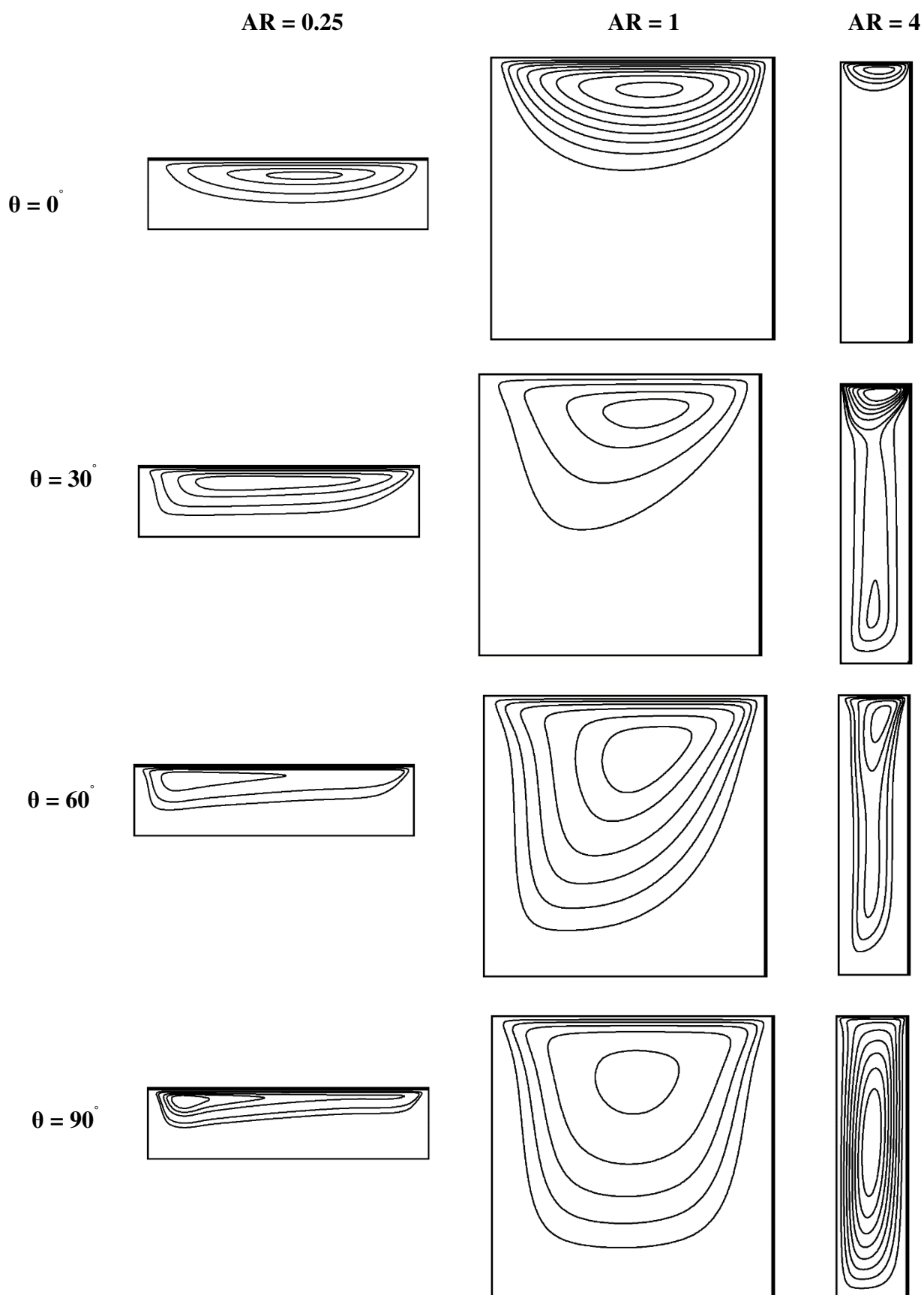


Fig. 13. Comparison of the streamlines for different aspect ratios and magnetic field angles at  $Bn = 1$ ,  $Ha = 5$ ,  $Ec = 10^{-3}$ , and  $Re = 100$

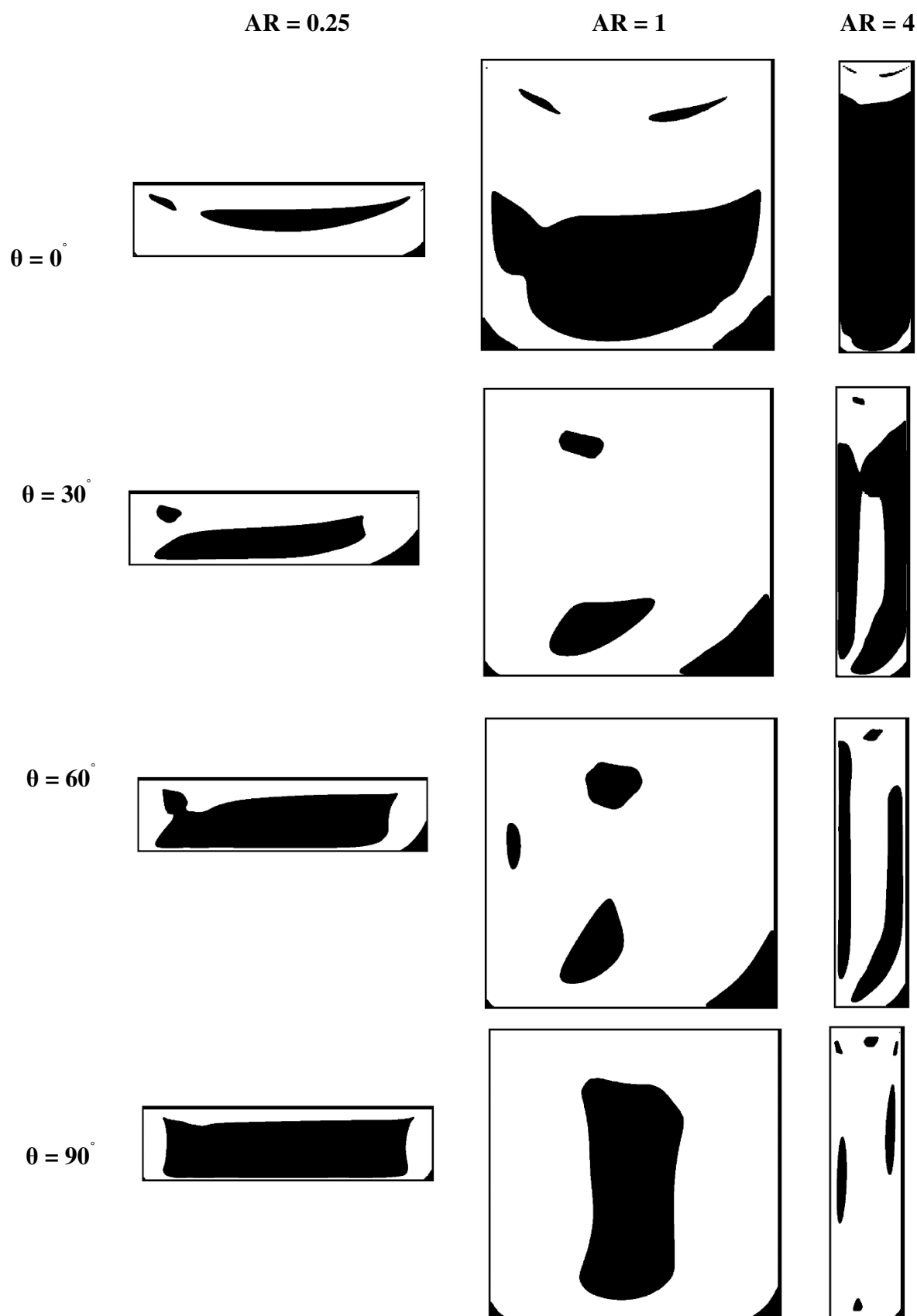


Fig. 14. Comparison of the yielded/unyielded parts for different aspect ratios and magnetic field angles at  $Bn = 1$ ,  $Ha = 5$ ,  $Ec = 10^{-3}$ , and  $Re = 100$

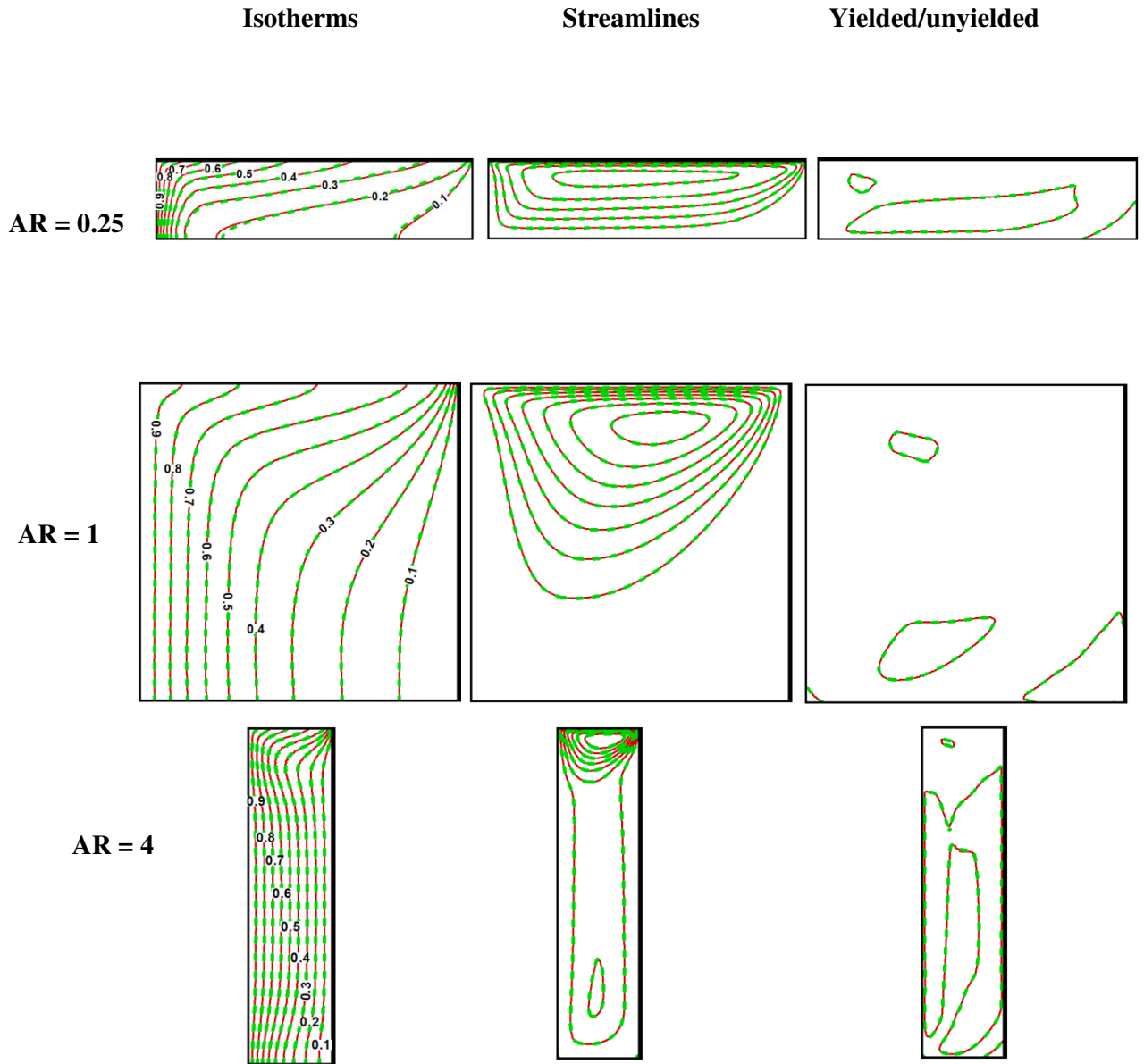


Fig. 15. Comparison of the isotherms, streamlines, yielded/unyielded sections for different aspect ratios and Eckert numbers at  $Bn = 1$ ,  $Ha = 5$ ,  $\theta = 30^\circ$ , and  $Re = 100$  (The solid red line ( $Ec = 0.01$ ), and the dashed green line ( $Ec = 10^{-4}$ ))